MHD SIMULATIONS OF GLOBAL ACCRETION DISKS WITH VERTICAL MAGNETIC FIELDS

Takeru K. Suzuki¹ & Shu-ichiro Inutsuka¹

Draft version July 18, 2018

ABSTRACT

We report results of three dimensional mangetohydrodynamical (MHD) simulations of global accretion disks threaded with weak vertical magnetic fields. We perform the simulations in the spherical coordinates with different temperature profiles and accordingly different rotation profiles. In the cases with a spatially constant temperature, because the rotation frequency is vertically constant in the equilibrium condition, general properties of the turbulence excited by magnetorotational instability (MRI) are quantitatively similar to those obtained in local shearing box simulations. On the other hand, in the cases with a radially variable temperature profile, the vertical differential rotation, which is inevitable in the equilibrium condition, winds up the magnetic field lines, in addition to the usual radial differential rotation. As a result, the coherent wound magnetic fields contribute to the Maxwell stress in the surface regions. Our global simulations give somewhat larger density fluctuation, $\delta\rho/\rho = 0.1 - 0.2$, near the midplane than the values obtained in previous local shearing box simulations and global simulations without net vertical magnetic field. The velocity fluctuations, dominated by the radial component, are $\approx 0.1 - 0.2$ of the local sound speed. The azimuthal power spectra of the magnetic fields show shallow slopes, $\propto m^0 \sim m^{-1}$, where m is an azimuthal mode number, which might be related to the energy injection by MRI from small scales. On the other hand, the power spectra of the velocities and density show steeper slopes, $\propto m^{-1} \sim m^{-2}$. We observe intermittent and structured disk winds driven by the Poynting flux associated with the MHD turbulence, with the slightly smaller mass fluxes than that obtained in our local simulations. The Poynting flux originating from magnetic tension is injected from the regions above a scale height toward both the midplane and the surfaces. Related to this, sound waves are directed to the midplane from the surface regions. The mass accretion mainly occurs near the surfaces and the gas near the midplane slowly moves outward in the time domain of the present simulations. The vertical magnetic fields are also dragged inward in the surface regions, while they stochastically move outward and inward around the midplane. The difference of the velocities at the midplane and the surfaces might cause large-scale meridional circulations. Applying to protoplanetary disks, these waves and circulation are supposed to play an important role in the dynamics of solid particles. We also discuss an observational implication of induced spiral structure in the simulated turbulent disks.

Subject headings: accretion, accretion disks — ISM: jets and outflows — magnetohydrodynamics (MHD) — protoplanetary disks — stars: winds, outflows — turbulence

1. INTRODUCTION

Magnetohydrodynamical (MHD) turbulence is believed to play a central role in the transport of the angular momentum and the mass in accretion disks (Balbus & Hawley 1998, and reference therein). Magnetorotational instability (MRI; Velikhov 1959; Chandrasekhar 1961; Balbus & Hawley 1991) is a promising mechanism that drives MHD turbulence in accretion disks. To date various attempts have been carried out to understand fundamental properties of MRI-driven turbulence. MHD simulations with local shearing boxes have been extensively performed (Hawley et al. 1995; Matsumoto & Tajima 1995; Brandenburg et al. 1995; Stone et al. 1996; Turner et al. 2003; Sano et al. 2004; Suzuki & Inutsuka 2009; Hirose et al. 2009; Shi et al. 2010; Davis et al. 2010; Suzuki et al. 2010). One of the important findings by local MHD simulations is that the net vertical magnetic field controls the saturation level of the turbulence (Hawley et al. 1995; Sano et al. 2004; Pessah et al. 2007; Suzuki & Inutsuka 2009; Okuzumi & Hirose

stakeru@nagoya-u.jp

¹ Department of Physics, Nagoya University, Nagoya, Aichi 464-8602, Japan

2011), which essentially determines the strength of the transport of angular momentum and resulting mass accretion.

On the other hand, the shearing box approximation is somewhat too idealistic since various effects that are important in realistic accretion disks are neglected. For instance, mass accretion cannot be handled in the shearing box treatment; instead the accretion rate is simply estimated from the transported angular momentum under the time-steady condition. In order to study realistic accretion disks, global MHD simulations have also been performed recently (Machida et al. 2000; Hawley 2000; Papaloizou & Nelson 2003; Machida & Matsumoto 2003; Nishikori et al. 2006; Fromang & Nelson 2006; Beckwith et al. 2009; Flock et al. 2011, 2012; Fromang et al. 2011, 2013; Hawley et al. 2011, 2013; Parkin & Bicknell 2013a,b). However, global simulations of accretion disks threaded with vertical magnetic fields have not been extensively performed except for a limited number of attempts (e.g. Beckwith et al. 2009).

In this paper, we investigate properties of MHD turbulence in accretion disks threaded with weak vertical magnetic fields by global MHD simulations. In global

disks the rotation profile in the equilibrium condition is determined by the distribution of density and temperature. In general, the rotation frequency changes in the vertical direction, in addition to the radial direction, unless the gas pressure satisfies a barotropic equation of state, $p = p(\rho)$ (generalization of von Zeipel (1924) theorem; e.g., Kozlowski et al. 1978; Maeder 1999, ; see §2.1). Then, the vertical magnetic fields are wound by the vertical differential rotation. In order to study this effect, we simulate disks with different temperature profiles.

This paper is organized as follows. In $\S 2$, we describe the setups of the global simulations. After presenting overall time evolutions ($\S 3$) and some snapshots of the disks ($\S 4$), in $\S 5$ we inspect details of MHD turbulence in the global accretion disks.

2. SIMULATION SETUPS

We simulate the time evolution of global accretion disks threaded by weak net vertical magnetic fields. Our simulations are performed in spherical coordinates, (r, θ, ϕ) and solve a following set of ideal MHD equations:

$$\frac{d\rho}{dt} + \rho \nabla \cdot \boldsymbol{v} = 0, \tag{1}$$

$$\rho \frac{d\mathbf{v}}{dt} = -\nabla \left(p + \frac{B^2}{8\pi} \right) + \left(\frac{\mathbf{B}}{4\pi} \cdot \nabla \right) \mathbf{B} - \rho \nabla \Phi \qquad (2)$$

and

$$\frac{\partial B}{\partial t} = \nabla \times (v \times B),\tag{3}$$

where the variables have the conventional meanings, and we take into account Newtonian gravity, $\Phi = -GM/r$, by a central object with mass M in Equation (2), but neglect the self-gravity in the accretion disks. We consider different temperature distributions described in §2.1. At each location we assume locally isothermal gas and do not solve an energy equation. Gas pressure, p, and density, ρ , are connected by sound speed, $c_{\rm s}$, which is spatially variable but constant with time as

$$p = \rho c_s^2. \tag{4}$$

For the data analyses, we mainly use cylindrical coordinates, (R, ϕ, z) . To do so, we convert data in the (r, θ, ϕ) coordinates to the (R, ϕ, z) coordinates.

We modify the simulation code used for the simulations in local shearing boxes (Suzuki & Inutsuka 2009; Suzuki et al. 2010) to handle global disks in the spherical coordinates. The adopted scheme is 2nd order Godunov-CMoCCT method (Sano et al. 1999), in which we solve nonlinear Riemann problems with magnetic pressure at cell boundaries for compressive waves (Iwasaki & Inutsuka 2011) and adopt the consistent method of characteristics (CMoC) for the evolution of magnetic fields (Clarke 1996; Stone & Norman 1992) under the constrained transport (CT) scheme (Evans & Hawley 1988) for the conservation of magnetic flux. We use the CFL condition of 0.3 for the time update in all the cases.

The accretion disks are set up in the simulation box that extends in $\theta = \frac{\pi}{2} \pm 0.5$. The radial and azimuthal sizes of each model are summarized in Table 1. The difference between Cases I and II is the temperature profile (see §2.1); in Case I the radial box is only in < $25r_{\rm in}$ because the equilibrium rotation profile does not exist

in the outer region; in Case II we use a very large box size, $> 400r_{\rm in}$, where $r_{\rm in}$ is the inner radius of the simulation box, to avoid effects of the unphysical reflection at the outer boundary. We use homogeneous grid spacing, $\Delta\theta$ and $\Delta\phi$, in the θ and ϕ directions. The radial grid size, Δr , is set up in proportion to $\propto r$. Then, the ratio of the grid sizes in the r, θ , and ϕ directions, $(\Delta l_r, \Delta l_\theta, \Delta l_\phi) \equiv (\Delta r, r\Delta\theta, r\sin\theta\Delta\phi)$, is constant with r at the midplane, which is $(1:1:\pi)$ for low-resolution runs and $\approx (1:1.25:2)$ for high-resolution runs (Table 1).

2.1. Initial Condition

The gas pressure is initially distributed with a powerlaw dependence on r at the midplane, $\theta = \pi/2$, of the disks,

$$p_{\rm mid} = p_{\rm in, mid} \left(\frac{r}{r_{\rm in}}\right)^{-\mu},\tag{5}$$

where the subscript "in" denotes the inner boundary of the simulation box and the subscript "mid" denotes the midplane of the disks. In this paper we only consider cases with $\mu=3$. According to the adopted temperature distributions, the initial density and rotation profiles are determined to satisfy the equilibrium configuration as explained in §2.1.1 & §2.1.2. As a seed for MRI we include small perturbations in the three components of v with the amplitude equal to 5×10^{-3} of the local sound speed.

We set up the initial vertical magnetic fields,

$$B_z = B_{z,\text{in}} \left(\frac{R}{r_{\text{in}}}\right)^{-\mu/2},\tag{6}$$

to give a constant plasma $\beta_{z,\mathrm{mid}} = 8\pi p_{\mathrm{mid}}/B_z^2$, a ratio of gas pressure to magnetic pressure, at the midplane of the accretion disks. In this paper, we simulate cases with initial $\beta_{z,\mathrm{mid}} = 10^5$. In order to set up the initial straight vertical field lines in the spherical coordinates exactly satisfying $\nabla \cdot \boldsymbol{B} = 0$ within the accuracy of round-off errors, we use the ϕ component of the vector potential (see the Appendix).

We initially set up the equilibrium configurations of the accretion disks by taking into account the force balance of the gas component while neglecting the magnetic pressure since the initial B_z is quite small. We perform simulations with two types of temperature distributions: $T={\rm const.}$, which we call Case I, and $T\propto 1/r$, which we call Case II. The most important difference between the two cases is the difference of the rotation profiles of the equilibrium configurations. If we neglect the effect of the magnetic fields, an equilibrium rotation profile of a differentially rotating accretion disk is derived from the force balance among the gas pressure, the centrifugal force, and the gravity of Equation (2) in the (R-z) plane of the cylindrical coordinates,

$$-\frac{1}{\rho}\frac{\partial p}{\partial R} + R\Omega^2 - \frac{\partial \Phi}{\partial R} = 0, \tag{7}$$

and

$$-\frac{1}{\rho}\frac{\partial p}{\partial z} - \frac{\partial \Phi}{\partial z} = 0, \tag{8}$$

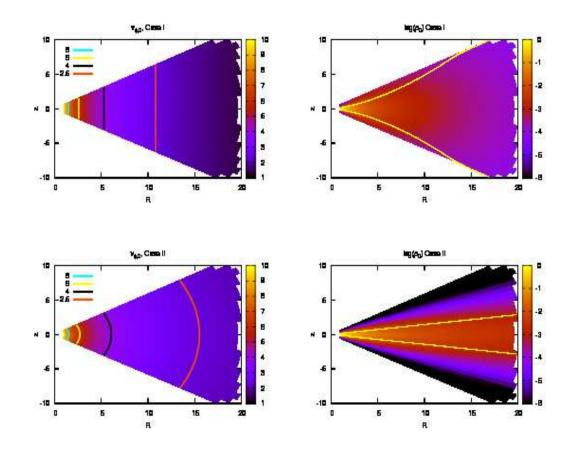


Fig. 1.— Initial condition of Case I (T = const.; upper) and Case II $(T \propto 1/r; lower)$ in an (R, z) plane. The left panels compare the rotation velocities of the two cases. The right panels compare the densities, where the yellow lines correspond to the locations of 1 scale height. In these figures, only the region inside $< 20r_{\text{in}}$ is shown.

TABLE 1 SIMULATION SETUPS.

Model	Simulation box (r, θ, ϕ)	Resolution (r, θ, ϕ)	Grid Size at midplane $\Delta l_r : \Delta l_{\theta} : \Delta l_{\phi}$	$(T \propto r^{-\nu})$	$\beta_{z,\mathrm{mid}}$	$t_{ m end} \ (t_{ m rot,in})$	$\Delta t_{ m ave} \ (t_{ m rot,in})$
I-high	$(1-25,\frac{\pi}{2}\pm0.5,0-\pi)$	(512,128,256)	$\approx 1:1.25:2$	0	10^{5}	600	200-300
II–high	$(1-640,\frac{\pi}{2}\pm0.5,0-\pi)$	(1024, 128, 256)	$\approx 1:1.25:2$	1	10^{5}	1830	1200 - 1800
I-low	$(1-22,\frac{\pi}{2} \pm 0.5,0-2\pi)$	(192,64,128)	$= 1 : 1 : \pi$	0	10^{5}	1000	300 – 500
II–low	$(1-470,\frac{\pi}{2}\pm0.5,0-2\pi)$	(384,64,128)	$=1:1:\pi$	1	10^{5}	2000	1200 – 2000

Note. — From left to right, tabulated are the name of models, a simulation box size, the numbers of grid points, the ratio of grid spacing at the midplane, the power law index of the temperature profile, the initial plasma β value at the midplane, the simulation time in unit of inner rotation time, and the duration for the time average.

where Ω is rotation frequency. Differentiating Equation (7) with z and Equation (8) with R, and subtracting them from each other, we have

$$-\frac{\partial}{\partial z} \left(\frac{1}{\rho} \frac{\partial p}{\partial R} \right) + \frac{\partial}{\partial R} \left(\frac{1}{\rho} \frac{\partial p}{\partial z} \right) + \frac{\partial}{\partial z} (R\Omega^2) = 0. \quad (9)$$

If gas pressure is globally barotropic, $p = p(\rho)$, the first and second terms are canceled out, hence,

$$\frac{\partial \Omega}{\partial z} = 0 \tag{10}$$

(von Zeipel (1924) theorem, e.g. Kozlowski et al. 1978).

In Case I the gas pressure satisfied a barotropic equation of state, and the rotation frequency is constant along the vertical direction, while in Case II the disks rotate differentially along the *vertical* direction in addition to the radial direction.

2.1.1. Case I

In Case I, we adopt constant temperature in the simulation box, namely the sound speed is constant everywhere:

$$c_{\rm s} = c_{\rm s,in} = 0.1 \sqrt{\frac{GM}{r_{\rm in}}} = {\rm const.},$$
 (11)

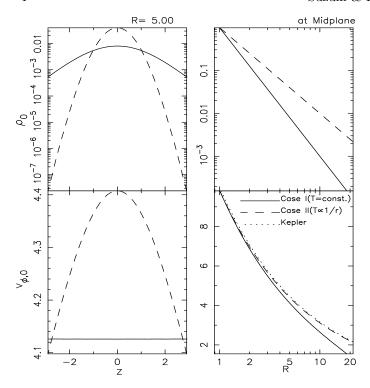


FIG. 2.— Comparison of the initial equilibrium structures of Case I (solid) and II (dashed). The density structures and the rotation velocities are plotted in the upper and lower panels, respectively. On the left the vertical (z) structures at R=5 are compared, and on the right the radial structures at the midplane are compared. In the bottom right panel, the Keplerian rotation speed is also compared (dotted).

which denotes that we set the ratio of the Keplerian rotation speed to the sound speed as 10 at the inner boundary, $r=r_{\rm in}$. The ratio decreases with R since the Keplerian rotation speed decreases. The initial density structure that satisfies the equilibrium configuration is given as

$$\rho = \rho_{\text{in,mid}} \left(\frac{R}{r_{\text{in}}}\right)^{-\mu} \exp\left[\frac{GM}{c_{\text{s}}^{2}} \left(\frac{1}{r} - \frac{1}{R}\right)\right]$$

$$\approx \rho_{\text{in,mid}} \left(\frac{R}{r_{\text{in}}}\right)^{-\mu} \exp\left[-\frac{GMz^{2}}{2R^{3}c_{\text{s}}^{2}}\right]$$

$$\equiv \rho_{\text{in,mid}} \left(\frac{R}{r_{\text{in}}}\right)^{-\mu} \exp\left[-\frac{z^{2}}{H^{2}}\right], \tag{12}$$

where note that $r = \sqrt{R^2 + z^2}$. This profile gives a familiar expression of the scale height², $H \approx \sqrt{2}c_{\rm s}/\Omega_{\rm K}$, where $\Omega_{\rm K}$ is the Keplerian frequency, $\Omega_{\rm K} = \sqrt{\frac{GM}{r^3}}$. Therefore, $H \propto R^{3/2}$, or

$$\frac{H}{R} = \sqrt{2}c_{\rm s,in} \left(\frac{R}{r_{\rm in}}\right)^{1/2} = 0.14 \left(\frac{R}{r_{\rm in}}\right)^{1/2}.$$
 (13)

 2 Note that instead of H in Equation (12), $H^{'}=c_{\rm s}/\Omega_{\rm K}(=H/\sqrt{2}),$ is often used (e.g., Fromang & Nelson 2006; Flock et al. 2011), which gives $\rho\propto \exp\left[-\frac{z^2}{2(H^{'})^2}\right]$

Our simulation box covers the spherical coordinates of $\theta = \pi/2 \pm 0.5$. Therefore, the vertical extent of the simulation box, $R \tan(\theta - \frac{\pi}{2})$, measured in H decreases with increasing R. At the inner boundary $R = r_{\rm in}$, the simulation box covers $\pm 4H$, but at $R = 10r_{\rm in}$ it covers $\approx \pm 1.3H$ (Figure 1). When analyzing the simulation data, we need to carefully take into account this effect. First, properties of the disk winds depend on the vertical box size in scale height (Suzuki et al. 2010; Fromang et al. 2013). Second, saturation levels of MRI-driven turbulence could depend on r because one scale height is resolved by larger numbers of θ (\approx vertical) grids for larger r.

For a given μ (= 3 throughout this paper) the rotation velocity, v_{ϕ} , is self-consistently determined as

$$v_{\phi}^2 = \frac{GM}{R} - \mu c_{\rm s}^2. \tag{14}$$

Here, this equation shows that because of the second term on the right-hand side the disks rotate with sub-Keplerian velocities. An important aspect of the rotation profile is that the rotation speed, v_{ϕ} , is a constant along the vertical direction and the direction of the differential rotation is exactly along the cylindrically radial direction, R (Figures 1 and 2). Therefore, vertical field lines are not wound up by shearing motions of the differential rotation, which is the most important difference from Case II described below.

Equation (14) indicates that the rotation velocity becomes 0 for a large R, because the radial force balance is satisfied between the gravity and the gas pressure without the contribution from the centrifugal force. For the adopted parameters, $\mu = 3$ and Equation (11), $v_{\phi} = 0$ at $R = 33r_{\rm in}$, because the gravity is solely supported by the gas pressure gradient. Outside of this radius, no equilibrium profile is achieved. Therefore, we set the simulation boxes for Cases I-high and I-low in $r < 30r_{\rm in}$ (Table 1).

In Case II, we consider the temperature distribution in proportion to 1/r, and then the sound speed has a dependence 3 ,

$$c_{\rm s}^2 = c_{\rm s,in}^2 \left(\frac{r}{r_{\rm in}}\right)^{-1},$$
 (15)

where $c_{s,in}$ is set to be 0.1 of the Keplerian rotation speed at r_{in} , which is the same as in Case I (Equation 11). In Case II the ratio of c_s to the Keplerian rotation speed is kept constant = 0.1 with r owing to the radial temperature gradient. We can derive a density structure and a rotation profile that satisfy the force balance:

$$\rho = \rho_{\rm in, mid} \left(\frac{r}{r_{\rm in}}\right)^{-\mu+1} \sin^{\nu} \theta, \tag{16}$$

and

$$v_{\phi}^2 = \nu c_{\rm s}^2,\tag{17}$$

 3 In previous studies, a similar temperature profile, $c_{\rm s} \propto R^{-1/2},$ which depends on cylindrical R instead of spherical r, is often adopted (e.g. Fromang & Nelson 2006; Flock et al. 2011, 2012). We do not believe that the difference significantly affects our simulation results.

where μ and ν satisfy

$$\mu + \nu = \frac{GM}{rc_s^2} = 100 (= \text{const.}),$$
 (18)

The comparison between Equations (17) and (18) shows that the rotation speed $v_{\phi} = \sqrt{\nu}c_{\rm s}$ is smaller than the Keplerian velocity, $r\Omega_{\rm K}$ because of the contribution from the gas pressure gradient to the force balance. In this paper, we adopt $\mu=3$ and accordingly $\nu=97$. A vertical scale height, H, can be approximately derived from Equation (16). We expand θ around $\theta=\frac{\pi}{2}$ assuming $\theta-\pi/2(\approx z/r)\ll 1$:

$$\sin^{\nu} \theta \approx 1 - \frac{\nu}{2} \left(\frac{z}{r}\right)^{2} \approx \exp\left(-\frac{\nu}{2} \left(\frac{z}{r}\right)^{2}\right)$$

$$\equiv \exp\left(-\frac{z^{2}}{H^{2}}\right), \tag{19}$$

where H is further transformed by using Equation (18) as

$$H^{2} = \frac{2r^{2}}{\nu} = \frac{2r^{2}c_{s}^{2}}{GM} \frac{\mu + \nu}{\nu} \approx \frac{2r^{2}c_{s}^{2}}{GM} = \frac{2c_{s}^{2}}{\Omega_{\nu}^{2}},$$
 (20)

which gives an asymptotic expression for H in Case II, similar to Equation (12) for Case I.

In contrast to Case I, in Case II $H \propto R$ from Equation (20), or

$$\frac{H}{R} = \sqrt{2} \frac{c_{\rm s}}{R\Omega_{\rm K}} = 0.14 \tag{21}$$

Thus, the vertical size, $R \tan(\frac{\pi}{2} \pm 0.5) = \pm 0.55R$, of the simulation box covers the constant scale height $\approx \pm 4H$ and H is resolved by the same number of θ grid points, which is independent of R. When analyzing the disk winds and the saturation levels of MRI turbulence, the setup for Case II is supposed to be more straightforward. Also in contrast to Case I, the equilibrium rotation profile exists even in the outer region. Thus, we take sufficiently large radial box sizes (470 for the low-resolution run and 640 for the high-resolution run; Table 1) to avoid unphysical wave reflection at the outer boundary, $r = r_{\text{out}}$. However, in this paper we mainly study the region inside $< 20r_{\rm in}$ because in the outer region the growth of the magnetic field, which is scaled by the rotation frequency, is slow and the saturated state is not achieved in the simulation time. In §6.1 we briefly discuss the time evolution in the entire region of Case II-high.

2.2. Boundary Condition

The boundary condition for the ϕ direction is straightforward. In the low-resolution runs, we treat the full (2π) disks and connect one edge to the other edge (technically, this is the same as the periodic boundary). In the high-resolution runs for the half (π) disks, we adopt a simple periodic boundary condition.

In the θ direction (\sim the vertical direction), we prescribe the outgoing boundary condition for mass and MHD waves by using the seven MHD characteristics (Suzuki & Inutsuka 2006), in order to handle disk winds (see also Suzuki & Inutsuka 2009; Suzuki et al. 2010).

We use a viscous accretion condition for the r direction,

which is a method adopted in Fromang & Nelson (2006)⁴. At both the inner and outer radial boundaries, we fix small v_r estimated from the α prescription for standard accretion disks (Shakura & Sunyaev 1973), $v_r = -\frac{3}{2}\frac{\alpha c_s^2}{r\Omega}$ with $\alpha = 5 \times 10^{-3}$. We fix v_θ and v_ϕ to the initial values, i.e., $v_\theta = 0$ and $v_\phi = \text{sub-Keplerian}$ rotation speed under equilibrium (Equations 14 & 17). The densities at the inner and outer radial boundaries are also fixed to the initial values. As for the magnetic fields, we assume the zero-gradient for $r^2(B_\theta^2 + B_\phi^2)$ across the boundaries, which nearly (not exactly) corresponds to the equilibrium from the magnetic pressure. The condition for the magnetic fields also allows flows of magnetic fluxes across the boundaries. Limitations for the prescribed boundary conditions will be discussed in §5.3 & 5.4.

2.3. Averaged Quantities

In order to quantitatively analyze numerical results, we take various kinds of averages of the obtained physical quantities. While we perform the simulations in the spherical coordinates (r, θ, ϕ) , the data are often analyzed in the cylindrical coordinates, (R, ϕ, z) . We take averages of a physical quantity, $A(t, R, \phi, z)$ in the following ways.

As an example, we explain how to derive a time- and ϕ -averaged vertical structure at a certain R (§5.1.1 & §5.2.1). The simple average of A is

$$\langle A \rangle_{t,\phi}(R,z) = \frac{\int_{\Delta t_{\text{ave}}} dt \int_{\phi_{\text{min}}}^{\phi_{\text{max}}} d\phi A}{\Delta t_{\text{ave}}(\phi_{\text{max}} - \phi_{\text{min}})}, \tag{22}$$

where the subscripts (t,ϕ) in this case) of the bracket correspond to the independent variables over which the average is taken and the rest (R,z) in this case) of the independent variables are written in the arguments. We integrate A over $\Delta t_{\rm ave}$ (Table 1) and in the entire region with respect to ϕ from $\phi_{\rm min}(=0)$ to $\phi_{\rm max}(=\pi)$ for the high-resolution runs and 2π for the low-resolution runs). In the denominator, the integration $(\int_{\Delta t_{\rm ave}} \int_{\phi_{\rm min}}^{\phi_{\rm max}} d\phi = \Delta t_{\rm ave}(\phi_{\rm max} - \phi_{\rm min}))$ is already carried out. In contrast to the simple average in Equation (22) the density-weighted average is derived as

$$\frac{\langle \rho A \rangle_{t,\phi}(R,z)}{\langle \rho \rangle_{t,\phi}(R,z)} = \frac{\int_{\Delta t_{\text{ave}}} dt \int_{\phi_{\text{min}}}^{\phi_{\text{max}}} d\phi \rho A}{\int_{\Delta t_{\text{ave}}} dt \int_{\phi_{\text{min}}}^{\phi_{\text{max}}} d\phi \rho}.$$
 (23)

For variables concerning magnetic field (§5.1.1), e.g., magnetic energy, $B^2/8\pi$, we take the simple average, Equation (22), and for variables concerning velocity (§5.2.1), e.g. flow speed, v, and kinetic energy per mass, $v^2/2$, we take the density-weighted average, Equation (23); in principle we take the average of a variable in units of energy density or momentum density.

To study the time evolution of overall trends in the

⁴ Fromang & Nelson (2006) also adopted a method with resistive buffer zones for both inner and outer radial boundaries for most of their simulations, which is different from the viscous accretion condition we use for our simulations. A reason why we adopt the viscous accretion condition is to avoid pileups of masses in the buffer zones for long-time simulations

disks (§3), we examine a box average.

$$\langle A \rangle_{R,\phi,z}(t) = \frac{\int_{\Delta R} R dR \int_{\Delta z} dz \int_{\phi_{\min}}^{\phi_{\max}} d\phi A}{\int_{\Delta R} R dR \int_{\Delta z} dz (\phi_{\max} - \phi_{\min})}, \quad (24)$$

where we integrate A in the entire region with respect to ϕ , but the regions for the R and z integrations, ΔR and Δz , are case-dependent and are explained later; in the denominator the integration with ϕ is carried out, but the integrations with R and z are left as they stand because Δz depends on R. As explained above we use variables in units per volume for A; for instance, to check a plasma $\beta (=8\pi p/B^2)$ value, we see $8\pi \langle p \rangle / \langle B^2 \rangle$, which essentially corresponds to the density-weighted average, rather than the simple volumetric average, $8\pi \langle p/B^2 \rangle$.

When we examine face-on snapshots of the disks ($\S4.1$), we take a vertical average,

$$\langle A \rangle_{z_{\text{tot}}}(t, R, \phi) = \frac{\int_{\Delta z_{\text{tot}}} dz A}{z_{\text{top}} - z_{\text{bot}}},$$
 (25)

over the entire region,

$$\Delta z_{\rm tot}: z_{\rm bot} \Rightarrow z_{\rm top}$$
 (26)

from the lower surface, $z_{\rm bot} = -R \tan(\theta_{\rm max} - \frac{\pi}{2})(<0)$, to the upper surface, $z_{\rm top} = -R \tan(\theta_{\rm min} - \frac{\pi}{2})(>0)$; note that the upper (lower) surface corresponds to the location at $\theta = \theta_{\rm min\;(max)} = \frac{\pi}{2} \mp 0.5$). For the analysis of time-averaged radial dependences (§5.1.2 & §5.2.2), we take the following average,

$$\langle A \rangle_{t,\phi,z}(R) = \frac{\int_{\Delta t} dt \int_{\Delta z} dz \int_{\phi_{\min}}^{\phi_{\max}} d\phi A}{\Delta t \Delta z(R) (\phi_{\max} - \phi_{\min})}, \tag{27}$$

where we do not only consider the whole region of $\Delta z_{\rm tot}$, but we also take the averages in regions near the midplane and surfaces. As for the midplane region, we consider the region in $z=\pm H$,

$$\Delta z_{\rm mid} : -H \Rightarrow H,$$
 (28)

and for the surface regions, we take averages over

$$\Delta z_{\rm sfc} : (z_{\rm bot} \Rightarrow \frac{3}{4} z_{\rm bot}) + (\frac{3}{4} z_{\rm top} \Rightarrow z_{\rm top}),$$
 (29)

where see §5.2.1 for an example.

In $\S5.1.3$ & 5.2.3 we evaluate azimuthal power spectra of magnetic fields, velocities, and density fluctuations (see Parkin & Bicknell (2013b) for 3D spectra from simulations in the spherical coordinates). We take the usual Fourier transformation of a variable A in the azimuthal direction.

$$A(t,R,m,z) = \frac{1}{\sqrt{2\pi}} \int A(t,R,\phi,z) e^{-im\phi} d\phi, \qquad (30)$$

where m has the relation of $m = Rk_{\phi}$ to the wave number, k_{ϕ} , in the ϕ direction. Then, we derive an azimuthal power spectrum after taking a simple average over time and R-z space.

$$\langle |A(m)^{2}| \rangle_{t,R,z} = \frac{\int_{\Delta t} dt \int_{\Delta R} dR \int_{\Delta z} dz |A^{2}(t,R,m,z)|}{\Delta t \int_{\Delta R} dR \int_{\Delta z} dz}.$$
(31)

Here $|A^2| = AA^*$, where A^* is the complex conjugate of

3. OVERVIEW OF TIME EVOLUTION

Figure 3 shows 3D views of time evolution of the 4 cases. The animations for these 4 cases up to $t_{\rm end}$ can be downloaded as online materials⁵. Cases I-low and I-high exhibit typical evolutions of MRI, initiated by the development of channel-mode flows, which are clearly seen in the panels at t = 50 inner rotations (the middle column). On the other hand, in Cases II-low and II-high the initial vertical magnetic field lines are strongly wound particularly in the surface regions by the vertical differential rotation. As a result, the configurations of the magnetic fields of Cases I & II look different at later times (right column); Cases I-high and I-low show more turbulent magnetic fields, while Cases II-high and II-low appear to be dominated by coherent magnetic fields wound by both radial and vertical differential rotation. From now on, we inspect the difference between the magnetic field structures as a result of the different temperature profiles and extensively discuss their outcomes in the following sections.

Figure 4 presents some representative quantities for the evolution of the disks. Here we focus on the physical quantities between $r_1 = 5r_{\rm in}$ and $r_2 = 10r_{\rm in}$; the region with $r < r_1$ is influenced by the inner boundary, particularly the decrease of the surface density by accretion and disk wind (§5); in the outer region, $r > r_2$, the magnetic fields are still in growth phases at the end of the simulations for Cases II-low and II-high because the dynamical time ($\propto r^{-3/2}$) is long there. From top to bottom in Figure 4, we compare the following quantities of the four cases: the mass in the entire region of $r_1 < r < r_2$ in spherical coordinates,

$$M(r_1 < r < r_2) = \int_{\phi_{\min}}^{\phi_{\max}} d\phi \int_{\theta_{\min}}^{\theta_{\max}} \sin\theta d\theta \int_{r_1}^{r_2} r^2 dr \rho,$$
(32)

the inverse of the plasma β value integrated in the midplane region of $\Delta z_{\rm mid}$ (Equation 28) in cylindrical coordinates,

$$\frac{1}{\langle \beta \rangle_{R,\phi,z_{\text{mid}}}(t)} \equiv \frac{\langle B^2 \rangle_{R,\phi,z_{\text{mid}}}(t)}{8\pi \langle p \rangle_{R,\phi,z_{\text{mid}}}(t)}$$
(33)

and the Maxwell stress normalized by gas pressure, which is integrated in the same region, $\Delta z_{\rm mid}$,

$$-\frac{\langle B_R B_z \rangle_{R,\phi,z_{\text{mid}}}(t)}{4\pi \langle p \rangle_{R,\phi,z_{\text{mid}}}(t)} \tag{34}$$

Note that they essentially correspond to the inverse of the density-weighted plasma β and the density-weighted nondimensional Maxwell stress.

The top panel of Figure 4 shows that the mass of Cases I-high and I-low decreases quite rapidly, while the mass of Cases II-high and II-low is rather constant. The rapid decreases seen in Cases I-high and I-low are mainly due to the mass loss caused by the disk winds from the surfaces. In these cases, the simulation box covers a smaller vertical scale height ($\approx \pm 1.8 H$ at $r_1 = 5 r_{\rm in}$ and $\approx \pm 1.3 H$ at $r_2 = 10 r_{\rm in}$) than the simulation box of Cases II-high and II-low. As discussed in Suzuki et al. (2010) and Fromang

 $^{^5}$ Animation files are also available at www.ta.phys.nagoyau.ac.jp/stakeru/research/glbdsk

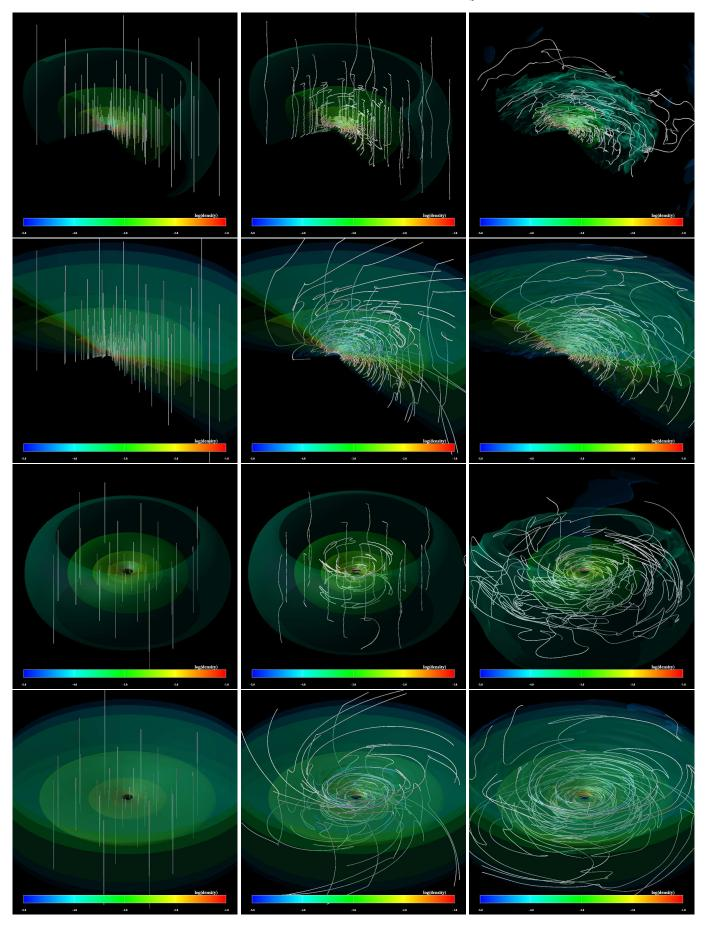


Fig. 3.— Time evolution of the 4 cases. From top to bottom displayed are Cases I-high, II-high, I-low, and II-low. From left to right, the results at $t=0,50,\,\&\,500$ inner rotations. White lines illustrate magnetic fields and colors indicate iso-density surfaces. Animations are available as online materials (also at www.ta.phys.nagoya-u.ac.jp/stakeru/research/glbdsk).

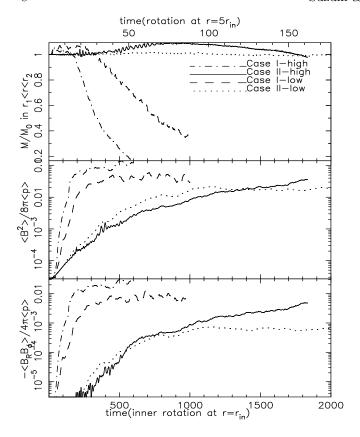


Fig. 4.— Time evolution of characteristic quantities of Case I-high (dash-dotted), Case II-high (solid), Case II-low (dashed), and Case II-low (dotted). On the horizontal axis, time is measured in units of inner rotation time at $r=r_{\rm in}$ on the bottom and in units of rotation time at $r=5r_{\rm in}$ on the top. Top: Mass in $r_1(=5r_{\rm in}) < r < r_2(=10r_{\rm in})$ normalized by the initial value. Middle: Volume-integrated magnetic energy in the midplane region, $\Delta z_{\rm mid}$, of $r_1 < r < R_2$, normalized by the volume-integrated gas pressure in the same region, $\frac{\langle B^2 \rangle_{R,\phi,z_{\rm mid}}(t)}{8\pi \langle p \rangle_{R,\phi,z_{\rm mid}}(t)},$ which essentially corresponds to the inverse of density weighted plasma β . Bottom: Volume-integrated Maxwell stress normalized by volume-integrated gas pressure, corresponding to density weighted nondimensional Maxwell stress. The integration is done in the same region as in the middle panel. (see text for the detail)

et al. (2013) by using MHD simulations in local shearing boxes (Hawley et al. 1995), the mass flux of the disk winds driven by MRI-triggered turbulence depends on the vertical box size; a smaller vertical box gives larger mass flux. In the present global simulations, a larger amount of the gas streams out of the θ surfaces of the simulation box of Cases I-high and I-low because of the insufficient vertical box size.

In Figure 5 we examine the actual supply/loss of the mass to/from the region of $r_1 < r < r_2$ for the high-resolution runs. The mechanisms are separated into two types, disk winds and radial flows. The mass loss caused by the disk winds can be measured via

$$\dot{M}_{\text{wind}}(r_1 < r < r_2) = \int_{\phi_{\text{min}}}^{\phi_{\text{max}}} d\phi$$

$$\int_{r_1}^{r_2} r dr [-(\rho v_{\theta} \sin \theta)_{\theta_{\text{min}}} + (\rho v_{\theta} \sin \theta)_{\theta_{\text{max}}}], \qquad (35)$$

where we take into account the disk winds from both the

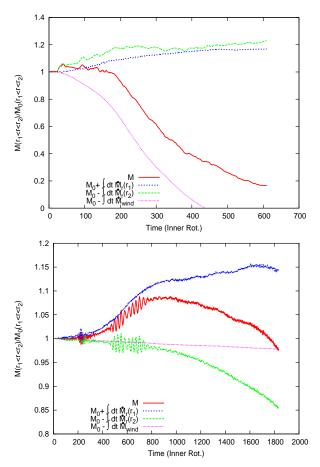


FIG. 5.— Evolution of the mass in $r_1(=5r_{\rm in}) < r < r_2(=10r_{\rm in})$ of Case I-high (upper panel) and Case II-high (lower panel). The mass normalized by the initial value, M_0 , (red solid) is compared with the case that only takes into account the mass supply from the inner radius (r_1) , $M_0 + \int dt \dot{M}_r(r_1)$ (blue short-dashed), the case with the mass supply from the outer radius (r_2) , $M_0 - \int dt \dot{M}_r(r_2)$ (greed long-dashed), and the case with the mass loss by the disk winds, $M_0 - \int dt \dot{M}_{\rm wind}$ (magenta dotted).

upper surface at $\theta = \theta_{\min} = \pi/2 - 0.5$ and the lower surface at $\theta = \theta_{\max} = \pi/2 + 0.5$. Note that $\dot{M}_{\rm wind}$ is defined in such a way that $\dot{M}_{\rm wind} < 0$ when the mass is lost by the disk winds $(v_{\theta}(\theta_{\min}) < 0 \text{ and } v_{\theta}(\theta_{\max}) > 0)$. As for radial flows, we measure the mass flux across a $\theta - \phi$ surface at $r(=r_1 \text{ or } r_2)$:

$$\dot{M}_r(r) = \int_{\phi_{\min}}^{\phi_{\max}} d\phi \int_{\theta_{\min}}^{\theta_{\max}} d\theta r^2 \sin \theta \rho v_r \qquad (36)$$

 $\dot{M}_r < 0$ for accretion $(v_r < 0)$. $\dot{M}_r(r_1) > 0$ and $\dot{M}_r(r_2) < 0$ contribute to an increase in the mass in $r_1 < r < r_2$, and vice versa.

Figure 5 shows that the disk winds continuously remove the mass ($\dot{M}_{\rm wind} < 0$) in both cases. $\dot{M}_{\rm wind}$ of Case II-high is considerably larger than $\dot{M}_{\rm wind}$ of Case II-high, mainly because the vertical extent of the simulation box per scale height is smaller in Case I as discussed previously. As a result, after 600 inner rotations, more than 80 % of the initial mass in $r_1 < r < r_2$ is lost in Case I-high. On the other hand, the effect of the mass loss caused by the disk winds is not as large in Case II-high.

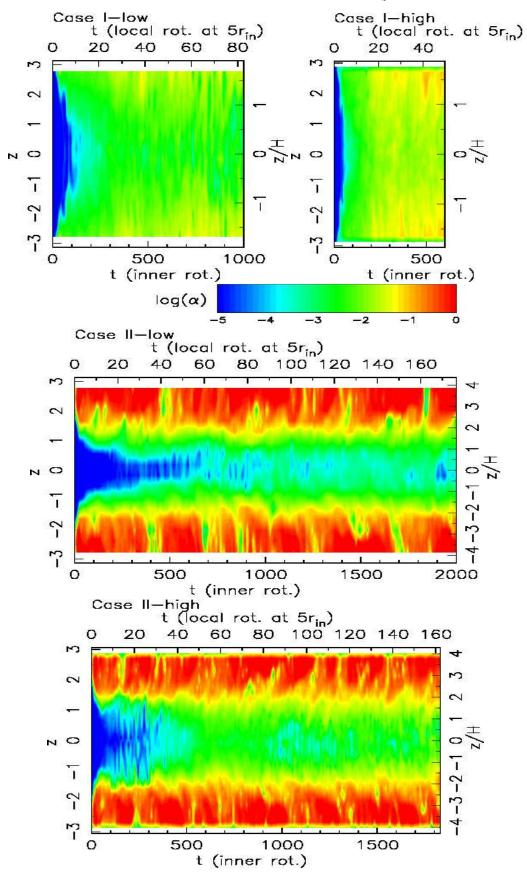


Fig. 6.— t–z diagrams of $\langle \alpha \rangle_{\phi}(r_1,z)$ at $R=r_1(=5r_{\rm in})$ for Case I-low (top-left), Case I-high (top-right), Case II-low (middle), and Case II-high (bottom). On the horizontal axis are shown time in the inner rotation (top of panels) and time in the local rotation at $r=r_1$ (bottom of panels). On the vertical axis are shown z (left) and z/H (right).

The radial flows show more complicated behaviors. In Case I-high, the mass is mostly supplied from the outer radius $(\dot{M}_r(r_2) < 0)$; green solid line) by accretion $(v_r < 0)$. From the inner radius $(r = r_1)$; blue short-dashed line), the mass is initially supplied to the simulation box by outward flows $(v_r > 0)$; $\dot{M}_r(r_1) > 0$) but eventually the mass is lost by accretion $(v_r < 0)$; $\dot{M}_r(r_2) < 0$.

On the other hand in Case II-high, the direction of the mass flow is initially outward $(v_r > 0)$ at both the inner and outer surfaces, namely the mass supply from $r = r_1$ (blue short-dashed line) and the mass loss from $r = r_2$ (green solid line). The radial flow at $r = r_2$ (green line) shows an oscillatory feature arising from epicycle motion during 400 - 800 inner rotations. At later times (t > 1600 inner rotations), the mass starts to accrete at $r = r_1$, while at $r = r_2$ the direction of the mass flow is kept outward. This tendency seems to follow the time evolution of a standard accretion disk (Lynden-Bell & Pringle 1974); the mass diffuses inward in the inner region and outward in the outer region from the diffusion center that gradually moves outward with time. As a result, at early time the mass supply from the inner radius, $r = r_1$, dominates the other components and the net mass increases up to $t \approx 800$ inner rotations, but later decreases by the disk winds and the radial outflow from the outer radius, $r = r_2$. We discuss radial mass flows in more detail in §5.4.

Turning back to Figure 4, the middle and bottom panels show the time evolution of properties of the magnetic fields, Equations (33) & (34). One of the characteristic features of the present simulations with net vertical fields is that the magnetic energy and Maxwell stress monotonically increase and seem to saturate but never systematically decrease because the strength of the net vertical field is kept more or less globally constant (see the discussion on the net β_z in §5.1). This is in contrast to global simulations without a net vertical magnetic flux, which exhibit a decrease of the magnetic energy caused by escaping net toroidal fields with vertical outflows after the initial amplification (e.g., Flock et al. 2011; Parkin & Bicknell 2013b).

In Cases I-low and I-high the magnetic fields are amplified more rapidly than in Cases II-low and II-high and are saturated after $t\gtrsim 200-300$ inner rotations or 20-30 local rotations at $r=5r_{\rm in}$. In all the cases our simulations cannot initially resolve the wavelengths,

$$\lambda_{\text{max}} \approx 2\pi \frac{B/\sqrt{4\pi\rho}}{\Omega},$$
 (37)

of the most unstable mode of MRI with respect to the initial magnetic field strength (Balbus & Hawley 1991). However, if Cases I and II are compared, one scale height can be resolved by a larger number of grid points in the outer regions of Cases I-high and I-low because of the dependence of the scale height, $H/R \propto R^{1/2}$ (Equation 13) as shown in Table 2. Thus, MRI in smaller scales, which correspond to faster growing modes, can be captured from the beginning, which leads to faster amplification of the magnetic fields in Cases I-high and I-low.

On the other hand, the magnetic fields in Cases II-high and II-low grow quite slowly, and are finally saturated after $t \gtrsim 1200$ inner rotations or $\gtrsim 110$ local rotations at $r = 5r_{\rm in}$, because the simulations cannot initially resolve

small-scale modes of MRI. With the increase of the magnetic field, $\lambda_{\text{max}}(\propto B)$ of the MRI increases, and can be marginally resolved at the midplane in Case II-high at later times, while it is underresolved for the R and z components at the midplane of Case II-low (see §5.1.1).

Comparing the high- and low-resolution runs, Cases I and II show a different trend. In Case I the high-resolution run shows the faster growth of the magnetic field and, consequently, a higher saturation level, which is expected from the amplification of the magnetic field by MRI; the higher-resolution run can resolve smaller scales with faster growth. On the other hand, in Case II the low-resolution run gives faster growth of the magnetic field, while the high-resolution run gives the higher saturation level. This indicates that a process other than from MRI operates in the amplification of the magnetic fields in Cases II-high and II-low. We suppose that the vertical differential rotation plays a key role, which will be discussed in §5.1.

In Figure 6, we present the α values,

$$\langle \alpha \rangle_{\phi}(t, r_1, z) = \frac{\langle \rho v_R \delta v_{\phi, 0} - B_R B_{\phi} / 4\pi \rangle_{\phi}(t, r_1, z)}{\langle p \rangle_{\phi}(t, r_1, z)}, \quad (38)$$

defined as the sum of Maxwell $(-B_R B_\phi/4\pi)$ and Reynolds $(\rho v_R \delta v_{\phi,0})$ stresses, at $R = r_1 (= 5r_{\rm in})$ in time (horizontal axis) – z (vertical axis) diagrams, where

$$\delta v_{\phi,0} = v_{\phi} - v_{\phi,0} \tag{39}$$

is the difference of the rotation speed from the initial equilibrium rotation speed, $v_{\phi,0}$. Note that using $\delta v_{\phi,0}$ to estimate the Reynolds stress might not be the best way because at later times the background rotation profile is modified by the change of the pressure gradient force due to the evolution of radial mass distribution. In the next section, we use the velocity shifts from the time-averaged v_{ϕ} rather than the initial $v_{\phi,0}$. However, the choice of the background v_{ϕ} does not affect the overall evolution of α since α is dominated by the Maxwell stress, and thus we simply use Equation (39) for Figure 6.

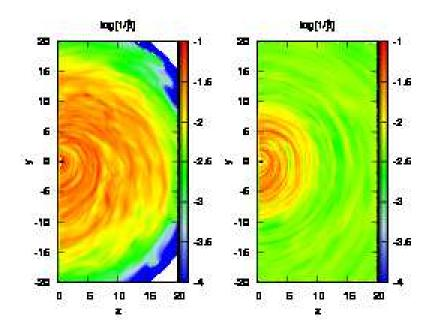
In all the cases, α starts to grow in the regions near the surfaces, $|z|\gtrsim 1.5$, which is similar to what is observed in our simulations with local shearing boxes (e.g. Suzuki & Inutsuka 2009). This is because the simulations can resolve $\lambda_{\rm max}$ there because of the smaller density and correspondingly larger $\lambda_{\rm max}$ than at the midplane. Around the midplane, α eventually increases and becomes saturated at later times, as discussed in Figure 4.

4. SLICE IMAGES

We investigate properties of the simulated accretion disks after the magnetic fields are amplified and saturated. In this section, we show typical slice images of the simulated accretion disks.

4.1. Face-on Views

Figure 7 illustrates snapshots of face-on views of the disks when the MHD turbulence is almost in the saturated state. For Cases I-low and I-high the snapshots at t=250 inner rotations are shown, and for Cases II-low and II-high we show the snapshots at t=1250 inner rotations. The colors indicate the inverse of the plasma β integrated with $\Delta z_{\rm tot}$ (Equation 26) in the entire z



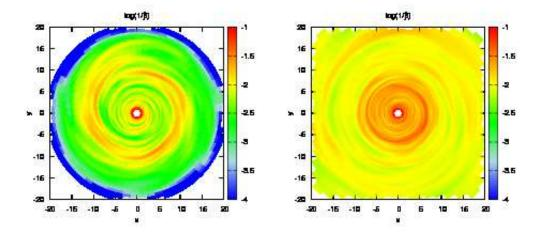


Fig. 7.— Face-on views of the simulated accretion disks of Case I-high at t=250 inner rotations (upper-left), Case II-high at t=1250 inner rotations (upper-right), Case II-low at t=250 inner rotations (lower-left), and Case II-low at t=1250 inner rotations (lower-right). Colors show $1/\langle \beta \rangle_{z_{\text{tot}}}$ in the logarithmic scale. Movies are available as online materials (also at www.ta.phys.nagoya-u.ac.jp/stakeru/research/glbdsk).

extent,

$$\frac{1}{\langle \beta \rangle_{z_{\text{tot}}}(t, R, \phi)} = \frac{\langle B^2 \rangle_{z_{\text{tot}}}(t, R, \phi)}{8\pi \langle p \rangle_{z_{\text{mid}}}(t, R, \phi)},\tag{40}$$

and brighter colors correspond to regions with relatively larger magnetic pressure. Winding structures dominate in Cases II-high and II-low, while both winding and turbulent structures are distributed in Cases I-high and I-low. Although these winding structures are not so long-lived with typical lifetimes of the order of rotation time, they are ubiquitously created somewhere in the disks (see Movies for Figure 7 available as *online materials* and at www.ta.phys.nagoya-u.ac.jp/stakeru/research/glbdsk).

4.2. Edge-on Views

Figure 8 presents edge-on views of the simulated disks in the saturated state. Here we present the results of only the high-resolution runs but zoomed-in views around the midplane (right panels) are displayed together with the views including the disk surfaces (left panels). Velocities normalized by the sound speed are shown by arrows, with the inverse of the plasma β in color. The velocity fields show a quite complicated structure with both radially inward $(v_R < 0)$ and outward $(v_R > 0)$ motions as well as vertical flows. Case II-high, which covers the larger vertical extent in scale height, captures detailed properties of the disk winds well. The zoomed-out panel for Case II-high (bottom left) shows that the velocities of the structured disk winds are about twice as fast as the local sound speed in some regions near the surfaces. The animation for the time-evolution of this figure ⁶ further shows these vertical outflows are intermittent with time.

5. PROPERTIES OF TURBULENT DISKS

For more quantitative studies of the magnetic fields and the turbulence in the disks, we examine several timeaveraged quantities. In order to study the saturated state, we consider the time average during Δt_{ave} summarized in Table 1. Although we perform the simulations of Cases I-high and I-low to $t_{\rm end} = 600$ and 1000 inner rotations respectively, a significant fraction of the mass is lost by the disk winds at later times (top panel of Figure 4), and the role of the magnetic field becomes relatively important (plasma β decreases), because the magnetic field is not as dissipated, as will be discussed in §5.4. Thus, we take the averages well before $t_{\rm end}$. As for Cases IIhigh and II-low, the mass is kept almost constant during the simulations as shown in Figure 4. Although the middle and bottom panels of Figure 4 show that in Case IIhigh the magnetic fields are still gradually growing during $\Delta t_{\rm ave}$, we take averages over $\Delta t_{\rm ave} = 1200 - 1800$ inner rotations because of the limitation of the computational

Figure 9 displays the surface density of the high-resolution runs averaged over Δt_{ave} and $\phi_{\text{min}} - \phi_{\text{max}}$:

$$\Sigma(R) = \frac{\int_{\Delta t_{\text{ave}}} dt \int_{\phi_{\text{min}}}^{\phi_{\text{max}}} d\phi \int_{z_{\text{bot}}}^{z_{\text{top}}} dz \rho}{\Delta t_{\text{ave}}(\phi_{\text{max}} - \phi_{\text{min}})}$$
(41)

 6 Time-evolution animations of Figure 8 are available at www.ta.phys.nagoya-u.ac.jp/stakeru/research/glbdsk

Model	$H/\Delta z_{\mathrm{mesh}}(r_1)$	$H/\Delta z_{\mathrm{mesh}}(r_2)$
Case I-high	35	51
Case I-low	18	25
Case II-high	16	16
Case II-low	8	8
Local	32	

TABLE 2 RESOLUTION OF EACH RUN AT $R=r_1(=5r_{\rm in})~(2nd~column)$ and $R=r_2(=10r_{\rm in})~(3rd~column).$

Note that the initial profiles, $\Sigma_0 \propto \rho_{\text{mid},0}H$, are

$$\Sigma_0 = \begin{cases} R^{-\frac{3}{2}} : \text{Case I} \\ R^{-1} : \text{Case II} \end{cases}$$
 (42)

In both cases, the mass in the inner region $r \lesssim 3r_{\rm in}$ is considerably lost by the accretion and the disk winds. On the other hand, the region in $r \gtrsim r_1 (=5r_{\rm in})$ is not so severely affected.

We now examine z and R dependences of various quantities. For the z dependence, we consider the average of Equation (22) at $R = r_1 (= 5r_{\rm in})$. For the radial dependence, we take the average of Equation (27), whereas for the integration of Δz , we consider (i) the midplane region, $\Delta z_{\rm mid}$ (Equation 28), and (ii) the entire region, $\Delta z_{\rm tot}$ (Equation 26). In Case II $\Delta z_{\rm tot}$ corresponds to $-4H \Rightarrow +4H$, while in Case I, $\Delta z_{\rm tot}$ measured in H varies with R since $H/R \propto R^{1/2}$ (Equation 13).

5.1. Magnetic Fields

In this subsection, we inspect various properties of the magnetic fields in the saturated state.

5.1.1. Vertical Structure at $5r_{\rm in}$

We examine the vertical structures of the magnetic fields at $R = r_1$, in comparison with results of a local shearing box simulation. As for the local simulation, we perform a 3D MHD simulation with the same strength for the net vertical field of $\beta = 10^5$ at the midplane as in the global simulations in a simulation box with the size, (x, y, z) = (2H, 4H, 8H), resolved by the uniform grid points of $(N_x, N_y, N_z) = (64, 128, 256)$ (see Suzuki et al. 2010, for the details); namely, one scale height, H, is resolved by 32 grid points. In Table 2, we summarize the resolution, $H/\Delta z_{\rm mesh}$, with respect to the vertical direction of each case, where Δz_{mesh} indicates the size of a vertical mesh. For the global simulations, we approximately use $\Delta z_{\rm mesh} \approx r\Delta\theta$. Although at the inner radius, $R = r_{in}$, the same resolution is set for Cases I and II, Case I gives a higher resolution at $R = r_1$ because of the different scalings of H/R (Equations 13 & 21).

Figure 10 compares the magnetic energies of each component of the four cases. We present here

$$\frac{\langle B_i^2 \rangle_{t,\phi}(r_1,z)}{4\pi p_{\text{mid},0}},\tag{43}$$

of *i*-th components ($i=R, \phi$, and z from left to right), where the normalization in the denominator is the initial gas pressure, $p_{\mathrm{mid},0}$, at the midplane. The saturated B_R^2 (left panel) and B_z^2 (right panel) show roughly positive correlations with the resolution, $H/\Delta z_{\mathrm{mesh}}$ (Table 2), whereas Case II-high gives the higher saturations than

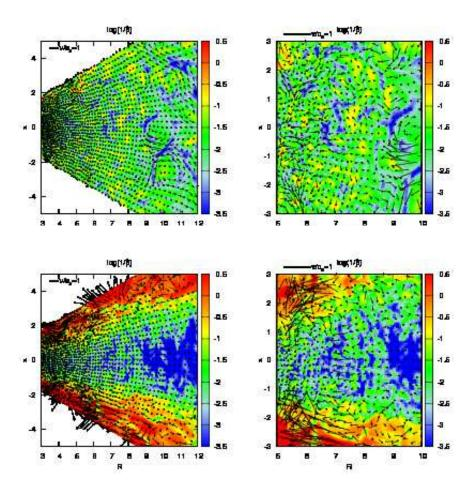


Fig. 8.— Edge-on views of the simulated accretion disks of Case I-high at t=250 inner rotations (upper) and Case II-high at t=1250 inner rotations (lower) at $\phi=\pi/4$. The right panels are zoomed-in views of the left panels to inspect the region near the midplane. Colors show $1/\beta$ in the logarithmic scale. The arrows indicate velocities normalized by the local sound speed, of which the scale is shown at the upper left corner of each panel. Time-evolution movies are available as online materials (also at www.ta.phys.nagoya-u.ac.jp/stakeru/research/glbdsk).

Case I-low though the $H/\Delta z_{\rm mesh}$ values are similar. In Case II-low (black dashed lines), which is the case with the lowest resolution at $R=r_1$, the strength of the magnetic field is too weak and shows a dip structure because of the insufficient resolution ($H/\Delta z_{\rm mesh}=8$) at the midplane. On the other hand, in Case I-high, which has a resolution similar to the local simulation, the saturated magnetic field strength at the midplane is comparable to that of the local simulation.

that of the local simulation. The dependence of B_{ϕ}^2 (middle panel of Figure 10) on the resolution is quite weak. Although Case I gives a positive dependence on the resolution, which is expected from the amplification by MRI, Case II shows complicated behavior; while in the midplane region, the high-resolution run gives larger B_{ϕ}^2 , in the surface regions, $|z| \gtrsim 1.5H$, the low-resolution run gives larger B_{ϕ}^2 . This indicates that the magnetic field strength in the surface regions of Case II is not regulated by the MRI but mainly by the vertical differential rotation, which does not have a positive dependence on the numerical resolution. This effect cannot be handled in local shearing box simulations, indicating the importance of studies using global

simulations.

In order to further study the amplification of the magnetic fields, in Figure 11 we inspect a quality factor, Q_i , of i—th components ($i=R,\phi,z$) for MRI (Noble et al. 2010; Hawley et al. 2011), which is defined as the ratio of the $\lambda_{\rm max}$ for MRI to a mesh size,

$$\langle Q_i \rangle_{t,\phi}(r_1,z) = 2\pi \frac{\sqrt{\langle v_{\mathrm{A},i}^2 \rangle_{t,\phi}(r_1,z)}}{\Omega \Delta l_i},$$
 (44)

where $\langle v_{A,i}^2 \rangle = \langle B_i^2 \rangle / 4\pi \langle \rho \rangle$ and we approximately use $\Delta l_i = \Delta r, r \sin\theta \Delta \phi$, and $r\Delta \theta$ for $i=R, \phi$, and z components, respectively, to convert the spherical coordinates used in the simulations to the cylindrical coordinates for the data analyses. According to Sano et al. (2004), $Q_z \gtrsim 6$ is a necessary condition for a vertical magnetic field to get a linear growth rate close to the analytic prediction from MRI.

The saturations of B_R^2 and B_z^2 shown in Figure 10 are well-explained by the profiles of Q_R (left panel) and Q_z (right panel) in Figure 11. In the midplane region of Case II-low $Q_R, Q_z < 1$, which leads to the low lev-

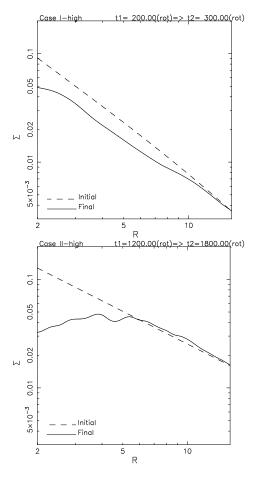


FIG. 9.— Surface density (solid lines) of Case I-high averaged during $\Delta t_{\rm ave} = 200-300$ inner rotations (upper) and of Case II-high averaged during $\Delta t = 1200-1800$ inner rotations (lower) in comparison with the initial value (dashed line).

els of B_R^2 and B_z^2 . Case I-high gives $Q_R,Q_z>10$ in the entire region, and then, the obtained saturation levels are supposed to be reasonable. In the other two cases, $Q_R,Q_z\approx 2-3$ at the midplane, which is probably marginally insufficient to resolve the MRI. Therefore, the saturation levels of these cases are lower than those of Case I-high and the local simulation. Since the toroidal component is amplified by the winding involving the differential rotation in addition to the MRI, $Q_\phi\gtrsim 5$ in the entire regions except in the midplane region of Case II-low.

Figure 12 presents the following four nondimensional quantities:

$$\frac{\langle B^2 \rangle_{t,\phi}(r_1,z)}{8\pi \langle p \rangle_{t,\phi}(r_1,z)} (= \frac{1}{\langle \beta \rangle_{t,\phi,}(r_1,z)}),\tag{45}$$

$$-\frac{\langle B_R B_\phi \rangle_{t,\phi}(r_1,z)}{4\pi \langle p \rangle_{t,\phi}(r_1,z)} : \text{ total Maxwell stress}, \qquad (46)$$

$$-\frac{\langle\langle B_R\rangle_{\phi}\langle B_{\phi}\rangle_{\phi}\rangle_{t}(r_1,z)}{4\pi\langle p\rangle_{t,\phi}(r_1,z)}: \text{ coherent Maxwell stress,}$$
(47)

$$\frac{\langle \rho v_R \delta v_\phi \rangle_{t,\phi}(r_1,z)}{4\pi \langle p \rangle_{t,\phi}(r_1,z)} : \text{ Reynolds stress}, \tag{48}$$

where the time average is taken over $\Delta t_{\rm ave}$ in Table 1. In Equation (47) we pick up the coherent part of the Maxwell stress in Equation (46), by taking the ϕ average of B_r and B_{ϕ} separately before multiplying them. This term is supposed to roughly correspond to the transport of angular momentum by magnetic braking (Weber & Davis 1967). The total Maxwell stress in Equation (46) contains both coherent and turbulent components. When estimating Reynolds stress, we use the difference of v_{ϕ} from the time-averaged value,

$$\delta v_{\phi} \equiv v_{\phi} - \langle v_{\phi} \rangle_{t,\phi} \equiv v_{\phi} - \frac{\langle \rho v_{\phi} \rangle_{t,\phi}}{\langle \rho \rangle_{t,\phi}}, \tag{49}$$

instead of the initial value (Equation 39) because the background rotation profile is slightly modified because of the change of the pressure gradient force through the evolution of radial density distribution, As shown in Equation (49), the background velocity, $\langle v_{\phi} \rangle_{t,\phi}$, is derived from the density-weighted average, $\langle \rho v_{\phi} \rangle_{t,\phi} / \langle \rho \rangle_{t,\phi}$.

The left panel of Figure 12 shows that the four cases mostly follow the trend of the local simulation; the plasma β values are $\approx 10-100$ at the midplane and decrease to < 1 in the surface regions owing to the decrease of the density by the gravity of the central object. The overall trends are similar for all these cases and only weakly depend on the resolution, because the total magnetic fields are dominated by the ϕ component, which weakly depends on the resolution. The magnetic field strengths in the surface regions of Cases II-high and II-low are larger than the value obtained in the local simulation, because the coherent magnetic fields are amplified by the vertical differential rotation.

The total Maxwell stress (the second panel from the left in Figure 12) around the midplane exhibits the positive dependence on the resolution, which is quite similar to B_R^2 and B_z^2 in Figure 10. The strength of the Maxwell stress near the midplane is determined by the MRI. On the other hand, the Maxwell stress in the surface regions of Cases II-high and II-low is considerably larger than that of the local simulation. Comparing the middle two panels, the Maxwell stress in the surface regions is mostly by the coherent component. The larger coherent Maxwell stresses in Cases II-high and II-low in the surface regions are a consequence of the wound-up magnetic field lines by the vertical differential rotation.

The Reynolds stress (the right panel of Figure 12) is systematically smaller than the Maxwell stress (second panel from the left) of each case by a factor of 2-3. The difference in the Reynolds stresses among the four models is similar to the tendency obtained for the total Maxwell stresses.

5.1.2. Radial Profile

Figure 13 compares the radial dependence of the i=R, z, and ϕ components of the t,ϕ,z averaged $\langle B_i^2 \rangle_{t,\phi,z}/4\pi$ of Case I-high (left panel) and Case II-high (right panel), where the z average is taken over the entire region, $\Delta z_{\rm tot}$. In both cases, the toroidal component dominates by the winding owing to the radial differential rotation, which is consistent with the result of previous local simulations (e.g., Suzuki et al. 2010). Examining quantitative ratios of different components, Case II-high gives larger $B_{\phi}^2/(B_z^2 + B_R^2)$ than Case I-high, because of the contri-

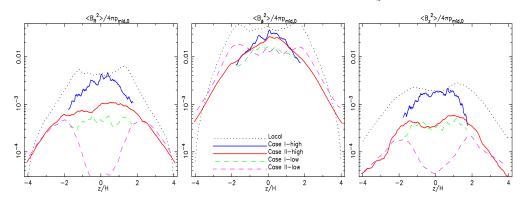


Fig. 10.— Vertical structures of $\langle B_i^2 \rangle_{t,\phi}(r_1,z)$ at $R=r_1(=5r_{\rm in})$ of Case I-high (blue solid), Case II-high (red solid), Case II-high (red solid), Case II-how (green dashed), and Case II-low (magenta dashed), in comparison with the result of the shearing box simulation (black dotted). From left to right, $i=R, \, \phi$, and z components are displayed.

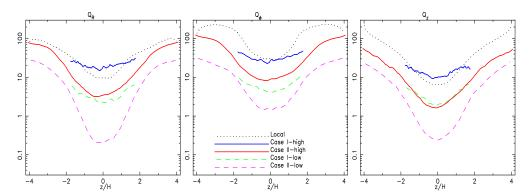


Fig. 11.— Vertical structure of the quality factors, Q_i , of the MRI, Equation (44), of Case I-high (blue solid), Case II-high (red solid), Case II-low (green dashed), and Case II-low (magenta dashed), in comparison with the result of the shearing box simulation (black dotted). From left to right, i = R, ϕ , and z components are displayed.

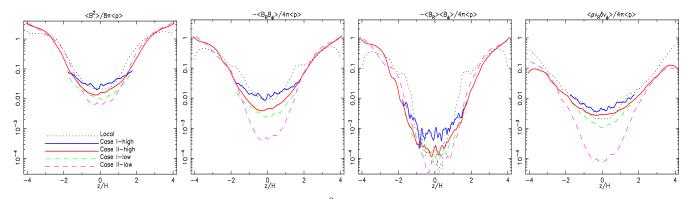


Fig. 12.— From left to right are shown vertical structures of $\frac{\langle B^2 \rangle_{t,\phi}(r_1,z)}{8\pi \langle p \rangle_{t,\phi}(r_1,z)}$, $-\frac{\langle B_R B_\phi \rangle_{t,\phi}(r_1,z)}{4\pi \langle p \rangle_{t,\phi}(r_1,z)}$ (total Maxwell stress), $-\frac{\langle \langle B_R \rangle_\phi \langle B_\phi \rangle_\phi \rangle_t(r_1,z)}{4\pi \langle p \rangle_{t,\phi}(r_1,z)}$ (coherent Maxwell stress), and $\frac{\langle \rho v_R \delta v_\phi \rangle_{t,\phi}(r_1,z)}{4\pi \langle p \rangle_{t,\phi}(r_1,z)}$ (Reynolds stress) of Case I-high (blue solid), Case II-high (red solid), Case II-low (green dashed), and Case II-low (magenta dashed), in comparison with the result of the shearing box simulation (black dotted). See Equations (45) – (48) for details.

bution from the vertical differential rotation.

Focusing on the radial dependences, the two cases give different trends. Here we again concentrate on the region between $R = r_1 (= 5r_{\rm in})$ and $R = r_2 (= 10r_{\rm in})$ to avoid effects of the inner boundary. Starting from the initial vertical fields with $B_{z,0}^2 \propto R^{-3}$, each component of Case I-high is amplified as it approaches R^{-2} , which is expected from the force balance between magnetic hoop

stress and magnetic pressure (Flock et al. 2011),

$$F = \frac{1}{\rho R^2} \frac{\partial}{\partial R} \left(R^2 \frac{B_\phi^2}{8\pi}\right) = 0. \tag{50}$$

 B_R^2 and B_z^2 , which are not explained by the force balance, are supposed to be subject simply to the largest ϕ component. On the other hand, each component of Case II-high is amplified while keeping the initial profile

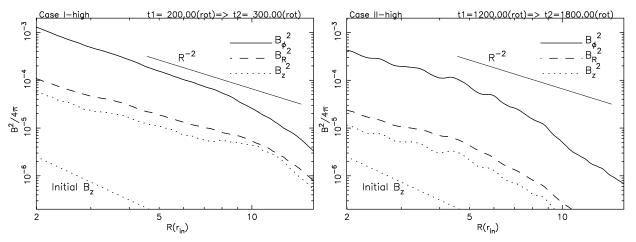


FIG. 13.— $\langle \frac{B_R^2}{4\pi} \rangle_{R,\phi,z_{\rm tot}}$ (solid), $\langle \frac{B_z^2}{4\pi} \rangle_{R,\phi,z_{\rm tot}}$ (dashed), and $\langle \frac{B_\phi^2}{4\pi} \rangle_{R,\phi,z_{\rm tot}}$ (dash-dotted) of Case I-high (left) and Case II-high (right). A slope, R^{-2} , (thin solid) and the initial condition, $\frac{B_z^2}{4\pi} = 2 \times 10^{-5} \left(\frac{R}{r_{\rm in}}\right)^{-3}$, (dotted) are overplotted. The vertical averages are taken over the entire region, $\Delta z_{\rm tot}$.

 $\propto R^{-3}$, whereas the magnetic field quickly decreases with R in $R > 10r_{\rm in}$ because it is still in the growth phase. The $\propto R^{-3}$ profile corresponds to the constant plasma β with R, as will be discussed below.

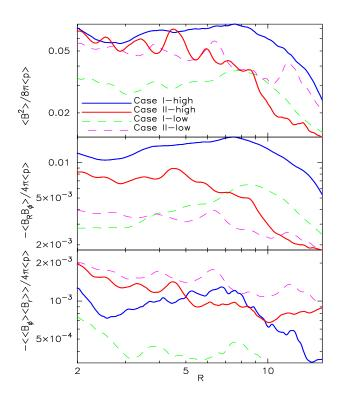


FIG. 14.— $\langle B^2 \rangle_{t,\phi,z_{\rm tot}}/4\pi \langle p \rangle_{t,\phi,z_{\rm tot}}$ (top) and total $(-\langle B_R B_\phi \rangle_{t,\phi,z_{\rm tot}}/4\pi \langle p \rangle_{t,\phi,z_{\rm tot}};$ middle) and coherent $(-\langle \langle B_R \rangle_\phi \langle B_\phi \rangle_{t,z_{\rm tot}}/4\pi \langle p \rangle_{t,\phi,z_{\rm tot}};$ bottom) components of Maxwell stress of Case I-high (blue solid), Case II-high (red solid), Case II-low (green dashed), and Case II-low (magenta dashed). In these plots, the integrations with z are performed in the entire vertical extent, $\Delta z_{\rm tot}$.

Figure 14 compares, from top to bottom
$$\frac{\langle B^2 \rangle_{t,\phi,z_{\text{tot}}}}{8\pi \langle p \rangle_{t,\phi,z_{\text{tot}}}} (= \frac{1}{\langle \beta \rangle_{t,\phi,z_{\text{tot}}}}), -\frac{\langle B_R B_\phi \rangle_{t,\phi,z_{\text{tot}}}}{4\pi \langle p \rangle_{t,\phi,z_{\text{tot}}}}, \text{ and}$$

 $-\frac{\langle\langle B_R\rangle_{\phi}\langle B_{\phi}\rangle_{\phi}\rangle_{t,z_{\text{tot}}}}{4\pi\langle p\rangle_{t,\phi,z_{\text{tot}}}}$, which are the vertically integrated quantities in Δz_{tot} in Equations (45) – (47) for the vertical structures (Figure 12).

 $\langle B^2 \rangle / 8\pi \langle p \rangle$ of Cases I-high (blue solid) and I-low (green dashed) show increasing trends with R in $R < 8r_{\rm in}$, while those of Case II-high (red solid) and II-low (magenta dashed) show slightly decreasing trends with R. The scalings of $\langle B^2 \rangle / 4\pi$ (Figure 13 for the high resolution runs) and $\langle B^2 \rangle / 4\pi \langle p \rangle$ in Figure 14 are different by the scaling of $\langle p \rangle$, which is proportional to $(\Sigma/H)c_{\rm s}^2$. In all the cases the final profiles of Σ (Figure 9) and correspondingly the profiles of $\langle p \rangle \propto R^{-\xi_p}$ become slightly shallower with $2.5 < \xi_p < 3$ in $r_1 < R < r_2$ than the initial profile, $\langle p \rangle \propto R^{-3}$. Therefore, the obtained trend, $\langle B^2 \rangle / 8\pi \propto R^{-\xi_B}$, with a shallower index $\xi_B \approx 2$ in Case I-high (Figure 13) as well as I-low results in the trend of $\langle B^2 \rangle / 8\pi \langle p \rangle$ increasing with R (Figure 14). On the other hand, in Case II-high as well as II-low the initial profile of $\langle B^2 \rangle / 8\pi$ with $\xi_B \approx 3$ is almost maintained (Figure 13), and the slow decreasing trend of $\langle B^2 \rangle / 8\pi \langle p \rangle$ results (Figure 14).

The Maxwell stresses (middle panel of Figure 14) follow the trends of $\langle B^2 \rangle / 8\pi \langle p \rangle$ (top panel): increasing with R in Cases I-high and I-low, and flat or slightly decreasing with R in Cases II-high and II-low. The coherent component of the Maxwell stresses (bottom panel of Figure 14) show different behaviors. In Cases I-high and I-low, the contributions from the coherent component are quite small. On the other hand, in Cases II-high and II-low, the roles of the coherent component are not negligible because of the vertical differential rotation of the equilibrium profile, and their radial dependences almost follow those of the total Maxwell stresses.

Comparing the high- and low-resolution runs, Cases I and II give totally different results. These three quantities of Case I-high (blue solid lines in Figure 14) are larger than those of Case I-low (dashed green lines), which is understandable from the amplification of the magnetic field by the MRI. The low-resolution run cannot resolve smaller-scale turbulence by the MRI, which leads to the smaller saturation level (Figure 11). On the other hand,

the comparison between the high- (red solid lines in Figure 14) and low-resolution (magenta dashed lines) runs of Case II shows a different trend. Although the higher saturation level of the Maxwell stress is obtained in the high-resolution run (middle), the coherent component of the Maxwell stress (bottom) shows the opposite behavior. The saturation of the total B^2 (top), which is dominated by B_{ϕ}^2 , looks almost independent of the resolution. These tendencies imply that, in addition to the MRI, the vertical differential rotation plays a role in the amplification of the magnetic fields in Cases II-high and II-low, which is consistent with the tendency obtained from the vertical structures (Figure 12).

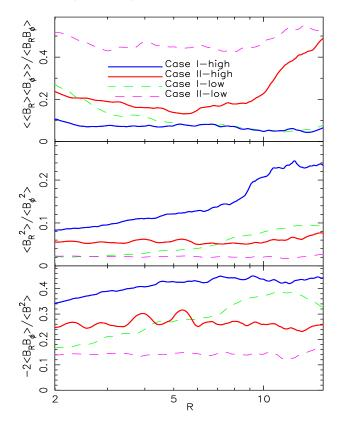


FIG. 15.— Ratios of various quantities concerning the magnetic fields of Case I-high (blue solid), Case II-high (red solid), Case II-low (green dashed), and Case II-low (magenta dashed). In these plots, the integrations with z are performed in the entire vertical extent, $\Delta z_{\rm tot}$. top: Relative contribution of the coherent component to the total Maxwell stress. $middle: \langle B_R^2 \rangle_{t,\phi,z_{\rm tot}}/\langle B_\phi^2 \rangle_{t,\phi,z_{\rm tot}}$. bottom: Maxwell stress, $-\langle B_R B_\phi \rangle_{t,\phi,z_{\rm tot}}/4\pi$, to magnetic pressure $\langle B^2 \rangle_{t,\phi,z_{\rm tot}}/8\pi$.

In Figure 15, we compare nondimensional quantities concerning magnetic fields. The top panel of Figure 15 compares the ratio of the coherent to total Maxwell stresses, $\langle \langle B_R \rangle_{\phi} \langle B_{\phi} \rangle_{\phi} \rangle_{t,z_{\text{tot}}} / \langle B_R B_{\phi} \rangle_{t,\phi,z_{\text{tot}}}$, which indicates the relative importance of the winding of magnetic field lines in the Maxwell stresses. The figure shows that this quantity has a negative correlation with the quality factor Q_i (Equation 44). For instance, Case II-low, which has the smallest Q (Figure 11), gives the largest $\langle \langle B_R \rangle_{\phi} \langle B_{\phi} \rangle_{\phi} \rangle_{t,z_{\text{tot}}} / \langle B_R B_{\phi} \rangle_{\phi,t,z_{\text{tot}}}$ among the four cases. In this case the total Maxwell stress is the smallest because of the insufficient resolution for the MRI, which

leads to the relatively large contribution of the coherent component by the winding. In addition to the dependence on the resolution, the vertical differential rotation originating from the temperature profile of Case II gives a larger fraction of the coherent component. Cases II-high and I-low give similar initial resolution, $H/\Delta_{z_{\rm mesh}}$, at $R=r_1$ (Table 2). Although Case II-high gives slightly larger Q there (see Figure 11), the fraction of the coherent component is larger there, which is the opposite of the tendency expected from the dependence on the resolution. This is also indirect evidence that in Case II-high the vertical differential rotation plays a role in the amplification of the magnetic field.

Hawley et al. (2011) introduced several diagnostics that are related to properties of MRI-driven turbulence in numerical simulations. In the middle and bottom panels of Figure 15 we show two such indices; the middle panel plots the ratio of the R component of the magnetic energies to the ϕ component R, $\langle B_R^2 \rangle_{t,z_{\text{tot}},\phi} / \langle B_\phi^2 \rangle_{t,z_{\text{tot}},\phi}$, and the bottom panel displays the ratios of the Maxwell stress to the magnetic pressure, which is defined as $\alpha_{\rm mag} = -2\langle B_R B_\phi \rangle/\langle B^2 \rangle$ in Hawley et al. (2011). These quantities, which exhibit similar trends, have positive correlations with the quality factor, which is the opposite of the trend obtained for $\langle\langle B_R\rangle_{\phi}\langle B_{\phi}\rangle_{\phi}\rangle_{t,z_{\rm tot}}/\langle B_RB_{\phi}\rangle_{\phi,t,z_{\rm tot}}$ in the top panel. Cases I-high (blue solid lines) and I-low (green dashed lines) show increasing trends with R, which reflects the adopted increasing trend of the numerical resolution, $H/\Delta z_{\rm mesh} \propto R^{1/2}$. On the other hand, Cases II-high (red solid lines) and II-low (magenta dashed lines), which have resolutions that remain constant with R, show rather flat trends with R.

On the basis of the shearing box simulations by Simon et al. (2011), $\langle B_R^2 \rangle / \langle B_\phi^2 \rangle$ approaches 0.2 with sufficient resolution. In the outer region of Case I-high, the value of $\langle B_R^2 \rangle_{t,z_{\rm tot},\phi}/\langle B_\phi^2 \rangle_{t,z_{\rm tot},\phi}$ is this saturation value, while the other cases give smaller $\langle B_R^2 \rangle_{t,z_{\rm tot},\phi}/\langle B_\phi^2 \rangle_{t,z_{\rm tot},\phi}$ probably because the resolution is not sufficient. However we need to carefully consider global effects such as radial flows, meridional flows and vertical differential rotation, which are not taken into account in local simulations. The vertical differential rotation in Cases II-high and II-low is supposed to give smaller $\langle B_R^2 \rangle_{t,z_{\rm tot},\phi}/\langle B_\phi^2 \rangle_{t,z_{\rm tot},\phi}$ because B_ϕ is systematically amplified.

The ratio of the Maxwell stress to the magnetic pressure, $-2\frac{\langle B_RB_\phi\rangle_{t,\phi,z_{\rm tot}}}{\langle B^2\rangle_{t,\phi,z_{\rm tot}}}$, also shows a positive correlation with the quality factor. Local simulations (Shi et al. 2010; Davis et al. 2010; Simon et al. 2011; Guan & Gammie 2011) with sufficient resolution give $-2\frac{\langle B_RB_\phi\rangle}{\langle B^2\rangle}\approx 0.3-0.4$ (Hawley et al. 2011). Case I-high gives a quite large value, $-2\frac{\langle B_RB_\phi\rangle_{t,\phi,z_{\rm tot}}}{\langle B^2\rangle_{t,\phi,z_{\rm tot}}}\approx 0.4$, while smaller values are obtained in the other cases. As we did for $\langle B_R^2\rangle/\langle B_\phi^2\rangle$, we also carefully take into account the global effects. Cases II-high and II-low are expected to give systematically lower $-2\frac{\langle B_RB_\phi\rangle_{t,\phi,z_{\rm tot}}}{\langle B^2\rangle_{t,\phi,z_{\rm tot}}}$, because the vertical differential rotation tends to increase B^2 through the amplification of B_ϕ^2 rather than $\langle B_RB_\phi\rangle$ through the coherent component $\langle B_R\rangle\langle B_\phi\rangle$ in a quantitative sense (Figure 12).

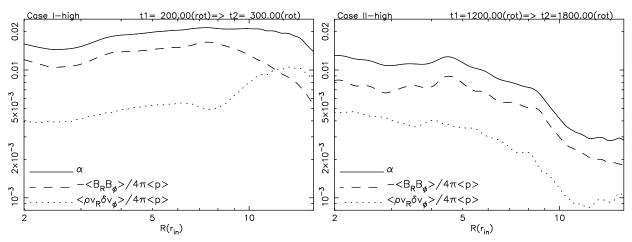


FIG. 16.— Maxwell stress $(-\langle B_R B_{\phi} \rangle_{t,\phi,z_{\text{tot}}}/4\pi \langle p \rangle_{t,\phi,z_{\text{tot}}}; dashed)$, Reynolds stress $(\langle \rho v_R \delta v_{\phi} \rangle_{t,\phi,z_{\text{tot}}}/4\pi \langle p \rangle_{t,\phi,z_{\text{tot}}}; dotted)$, and their sum, α , of Case I-high (*left*) and Case II-high (*right*). The vertical averages are taken over the entire region, Δz_{tot} .

Figure 16 compares the radial profiles of α values (solid lines),

$$\langle \alpha \rangle_{t,\phi,z_{\text{tot}}}(R) \equiv \frac{\langle \rho v_R \delta v_\phi \rangle_{t,\phi,z_{\text{tot}}}(R)}{\langle p \rangle_{t,\phi,z_{\text{tot}}}(R)} - \frac{\langle B_R B_\phi \rangle_{t,\phi,z_{\text{tot}}}(R)}{4\pi \langle p \rangle_{t,\phi,z_{\text{tot}}}(R)},$$
(51)

of Case I-high (left panel) and Case II-high (right panel). and their breakdowns to the Reynolds (dotted lines) and Maxwell (dashed lines) stresses, which are the first and second terms of Equation (51), respectively. Here δv_{ϕ} is the difference of the rotation velocity from the timeaveraged value, Equation (49). Although the Maxwell stresses are larger than the Reynolds stresses in both the cases, the ratios are slightly different. Case I-high gives a ratio of the Maxwell stress to Reynolds stress of $\approx 3:1$, while Case II-high gives $\approx 2:1$; both these values are smaller than the typical value of $\approx 5:1$ obtained in local shearing box simulations (Sano et al. 2004). However, we cautiously note that there are ambiguities particularly in the choice of δv_{ϕ} used to estimate the Reynolds stresses in the global simulations. Here we derive δv_{ϕ} by subtracting v_{ϕ} from the ϕ and Δt_{ave} -averaged v_{ϕ} (Equation 49). If we used a shorter duration for the time average, δv_{ϕ} would be smaller because $\langle v_{\phi} \rangle$ gradually changes with time owing to the change in the radial density profile. In this case the derived Reynolds stress would be smaller. Then, the above estimated ratios of the Maxwell stress to Reynolds stress are lower limits in a sense, and we need to be careful when comparing Reynolds stresses of global simulations with those of local simulations.

The dependence of the saturations of MRI-triggered turbulence on net vertical magnetic field strengths has been extensively studied by using local shearing box simulations to date, and it has been discussed that the net B_z plays an important role in determining the α parameter (Hawley et al. 1995; Matsumoto & Tajima 1995; Brandenburg et al. 1995; Sano et al. 2004; Hirose et al. 2006; Pessah et al. 2007; Suzuki & Inutsuka 2009; Okuzumi & Hirose 2011). Figure 17 shows the relation between the net vertical field strengths (horizontal axis) and the α values (vertical axis) derived from our global simulations. The net vertical magnetic flux at each R is not conserved in the global simulations because of radial motions of the field lines, in contrast to the treatment

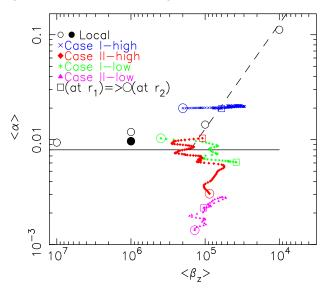


FIG. 17.— Dependence of time and ϕ -z plane averaged $\langle \alpha \rangle_{t,\phi,z_{\rm tot}}$ on plasma $\langle \beta_z \rangle_{t,\phi,z_{\rm tot}}$ for net vertical magnetic fields in $r_1 < R < r_2$. Multiple data points for each case of the global simulations correspond to different radial locations. Colored squares and circles indicate the data at $R = r_1$ and $R = r_2$. Case I-high (blue crosses), Case II-high (red diamonds), Case I-low (green asterisks), and Case II-low (magenta triangles) are compared with the local simulations by Suzuki et al. (2010, jopen circles for low-resolution runs and filled circle for high-resolution run). The solid line is a 'floor' value based on the local simulations and the dashed line is a fit for the increasing trend of $\langle \alpha \rangle$ (Suzuki et al. 2010).

by local shearing boxes in which the net vertical flux is strictly conserved within round-off errors. Thus, we derive the time-averaged net vertical field strength in the form of plasma β in the following way:

$$\langle \beta_z \rangle_{t,\phi,z_{\text{tot}}}(R) \equiv \frac{8\pi \langle p_{\text{mid}} \rangle_{t,\phi}(R)}{\langle \langle B_z \rangle_{t,\phi}^2 \rangle_{z_{\text{tot}}}(R)},\tag{52}$$

where we take the entire vertical box, $\Delta z_{\rm tot}$, for the z average of the net ϕ - and $\Delta t_{\rm ave}$ -averaged $\langle B_z \rangle_{t,\phi}$. The meaning of Equation (52) is probably straightforward. Net vertical field strength is first estimated by the ϕ and time average, which is squared before being integrated over $\Delta z_{\rm tot}$. The normalization is taken with the ϕ - and time-averaged gas pressure at the midplane. Note

that $\langle \beta \rangle_{t,\phi,z_{\rm tot}}(R)$ is also affected by the change of local density in addition to radial motions of vertical field lines. $\langle \alpha \rangle_{t,\phi,z_{\rm tot}}(R)$ (Equation 51) are plotted with the derived $\langle \beta \rangle_{t,\phi,z_{\rm tot}}(R)$ values in Figure 17, in comparison with the results of the local shearing box simulations by Suzuki et al. (2010). A number of the data points for each case of the global simulations correspond to different radial locations, and here we pick up the data in $r_1 \leq R \leq r_2$. The data points at $R = r_1$ and $R = r_2$ are indicated by squares and circles. The simulation box size for the local simulations adopted in Suzuki et al. (2010) is (x,y,z) = (H,4H,8H) (smaller than that used in §5.1.1), and the grid numbers are (32,64,256) for the low-resolution runs (open circles) and (64,128,512) for the high-resolution run (filled circle).

The saturation levels of $\langle \alpha \rangle_{t,\phi,z_{\rm tot}}$ are roughly correlated with the resolution (Table 2). Case I-high (blue crosses; $H/\Delta z_{\rm mesh}=35$ at $R=r_1$ and 51 at $R=r_2$) seems to capture MRI turbulence well and gives $\langle \alpha \rangle \approx 0.02$, which is comparable to the level obtained in the local simulations. On the other hand, Case II-low (magenta triangles; $H/\Delta z_{\rm mesh}=8$) does not resolve small-scale turbulence and $\langle \alpha \rangle$ is far below the floor value (= 8×10^{-3} ; solid line) based on the local simulations. In the outer region of Case II-high (red diamonds; $H/\Delta z_{\rm mesh}=16$), which is close to the red open circle at $R=r_2$, the turbulence is still supposed to be in the developing phase.

It seems that the global simulations do not show correlations of the saturated $\langle \alpha \rangle$ with the net vertical field strength. However, when examining the results of Cases I-high and I-low, we should carefully take into account the radial change of the resolution. For instance, in Case I-high (blue crosses), $\langle \alpha \rangle (r_2) \approx \langle \alpha \rangle (r_1)$ (squares for $R=r_1$ and circles for $R=r_2$), although the net vertical field strength at $R=r_2$ is weaker than at $R=r_1$ ($\langle \beta_z \rangle (r_2) > \langle \beta_z \rangle (r_1)$). This is partly because the scale height is resolved by the larger number of grid points at $R=r_2$ ($H/\Delta_{\rm mesh}z=51$) than at $R=r_1$ ($H/\Delta_{\rm mesh}=35$); a positive correlation of $\langle \alpha \rangle$ might be smeared out by the dependence on the resolution.

5.1.3. Azimuthal Power Spectra

In Figure 18 we present azimuthal power spectra of each component of the magnetic fields. We first take the Fourier transformation of $B_i/\sqrt{4\pi p}$ $(i=R,z,\phi)$ by using Equation (30). Then we derive the power spectrum from Equation (31) by taking the average over $\Delta z_{\rm mid}$ ($\pm H$ around the midplane; Equation 28), $\Delta R = r_1 \Rightarrow r_2$, and $\Delta t_{\rm ave}$. The azimuthal mode is covered from $m_1 = 1$ to $m_{\rm h} = 64$ in the low-resolution runs that cover the full 2π disk by 128 grid points. On the other hand, in the high-resolution runs that treat the half (π) disk by 256 grid points, the azimuthal mode is covered from $m_1 = 2$ to $m_{\rm h} = 256$. Since regions close to $m_{\rm h}$ are strongly affected by numerical dissipation, we focus on the regions in $m \lesssim m_{\rm h}/10$.

If MRI dominantly contributes to the generation of turbulent magnetic field, the injection scale is supposed to be comparable to the wavelength, λ_{max} , of the most unstable mode (Equations 37). The corresponding injec-

tion scale in terms of mode $m_{\rm inj}$ can be estimated as

$$m_{\rm inj} = Rk_{\phi,\rm inj} \approx R \frac{2\pi}{\lambda_{\rm max}} \approx \frac{2\pi/\Delta\phi}{Q_{\phi}}$$

 $\approx 50 \left(\frac{2\pi/\Delta\phi}{512}\right) \left(\frac{Q_{\phi}}{10}\right)^{-1},$ (53)

where we use the relation, $\lambda_{\text{max}} \approx Q_{\phi} \Delta l_{\phi} = Q_{\phi} R \Delta \phi$ (Equations 37 and 44), and the normalization in the second line is done for typical values of Case II-high. This estimate shows that the energy injection is from high m modes (small scales).

The R (left panel of Figure 18) and z (right panel) components show flat spectra in $m \lesssim m_h/10$. The ϕ component (middle panel) shows slightly steeper spectra with $\propto m^{-1}$, probably because large-scale (small m) fields are amplified by the winding due to the differential rotation. These obtained power spectra are shallower than theoretical predictions based on incompressible MHD turbulence consisting of Alfvénic wave packets (e.g., Goldreich & Sridhar 1995; Cho & Lazarian 2003). For example, Goldreich & Sridhar (1995) show that well-developed Alfvénic turbulence gives anisotropic power-law indices with respect to a background magnetic field with power $\propto k_{\perp}^{-5/3}$ and $\propto k_{\parallel}^{-2}$, where k_{\perp} and k_{\parallel} are wave numbers perpendicular and parallel to the background field. In the present global disk simulations, the magnetic fields are dominated by the ϕ component. Thus, we expect $m = Rk_{\phi} \approx Rk_{\parallel}$, and power $\propto m^{-2}$. A unique character of MRI in accretion disks is that the turbulent energy is injected from small scales (Equation 53). This is in contrast to the above picture for Alfvénic turbulence, in which the energy is injected from a large scale and cascades to smaller scales. This difference can explain the obtained shallow power spectra of the magnetic fields in the accretion disks.

5.2. Velocity & Density Fluctuations

We examine fluctuations of velocity and density here. Compared to magnetic fields, extracting the fluctuation components of velocity and density in global simulations is not straightforward, because of ambiguities in measuring the "average" quantities. In this paper, we use the ϕ - and time-integrated quantities as the average values. We begin with vertical structures at $R=r_1(=5r_{\rm in})$ and later inspect radial profiles in the same manner as in the previous subsection for the magnetic fields.

5.2.1. Vertical Structure at $R = 5r_{\rm in}$

We evaluate velocity fluctuations of the i-th component normalized by the local sound speed from the simulations by taking density weighted averages,

$$\frac{\sqrt{\langle \delta v_i^2 \rangle_{t,\phi}(r_1,z)}}{c_{\rm s}} \equiv \sqrt{\frac{\langle \rho \delta v_i^2 \rangle_{t,\phi}(r_1,z)}{\langle p \rangle_{t,\phi}(r_1,z)}},\tag{54}$$

where for the i=R component we simply use $\delta v_i = v_R$, and for the $i=\phi$ component $\delta v_{\phi} = v_{\phi} - \langle \rho v_{\phi} \rangle_{t,\phi} / \langle \rho \rangle_{t,\phi}$ (Equation 49). As for the i=z component we use the same subtraction from the averaged value,

$$\delta v_z = v_z - \langle v_z \rangle_{t,\phi} = v_z - \frac{\langle \rho v_z \rangle_{t,\phi}}{\langle \rho \rangle_{t,\phi}}$$
 (55)

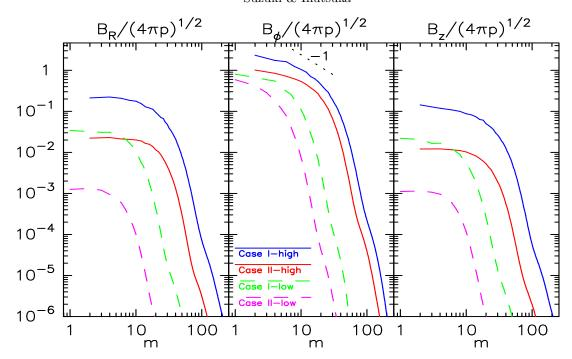


Fig. 18.— Azimuthal power spectra of nondimensional magnetic fields, $B/\sqrt{4\pi p}$, around the midplane of Case I-high (blue solid), Case II-high (red solid), Case I-low (green dashed), and Case II-low (magenta dashed). From left to right, the R, ϕ , and z components are displayed. The data are averaged over $\Delta z_{\rm mid}$, $\Delta R = r_1 \Rightarrow r_2$, and $\Delta t_{\rm ave}$. The low resolution runs (Cases I-low & II-low) cover m=1-64, and the high resolution runs (Cases I-high & II-high) cover m=2-256.

to remove the effect of the disk winds, which is not negligible in the regions near the surfaces (§5.3). We evaluate density fluctuations as the root mean squared difference from the time- and ϕ -averaged density:

$$\langle \frac{\delta \rho}{\rho} \rangle_{t,\phi}(r_1, z) \equiv \sqrt{\frac{\langle (\rho(t, r_1, \phi, z) - \langle \rho \rangle_{t,\phi}(r_1, z))^2 \rangle_{t,\phi}(r_1, z)}{(\langle \rho \rangle_{t,\phi}(r_1, z))^2}}$$
(56)

The time averages are again taken over $\Delta t_{\rm ave}$ (Table 1). The four panels of Figure 19 display the vertical structures of the three components of the velocity fluctuations and the density fluctuations. The four cases of the global simulations are compared with the local shearing box simulation (black dotted lines).

Three cases of the global simulations (all except Case II-low) give similar trends of the velocity fluctuations; the R component dominates the other components and the total fluctuations $\sqrt{\langle \delta v^2 \rangle}/c_{\rm s} \approx 0.1-0.2$ at the midplane increase towards the surfaces, where $\delta v^2 = v_R^2 + \delta v_\phi^2 + \delta v_z^2$. The fluctuation component is larger than the mean component of the mass flows, $\langle \rho v \rangle/\langle \rho \rangle$ (§5.3 & 5.4), by more than an order of magnitude near the midplane. Case II-low shows quite small velocity fluctuations at the midplane because MRI-triggered turbulence is not well developed there because of the insufficient resolution.

The R component of the velocity fluctuations in the midplane region of all the global cases except for Case II-low is systematically larger than the value obtained in the local simulation, while the z component is smaller. The global simulations can handle net radial flows, which cannot be taken into account in the local shearing box approximation. Such radial flows contribute to the obtained $\sqrt{\langle v_R^2 \rangle}/c_s$, in addition to the pure fluctuating

component.

The velocity fluctuations of Case II-high give a level similar to that of Case I-high, whereas the detailed profile is slightly different in each component. This is in contrast to the results where Case II-high gives a lower saturation of the magnetic field (Figures 10 & 12). This implies that global mass flows involving the vertical differential rotation contribute to the velocity fluctuations.

The density fluctuations (right-most panel of Figure 19) of all the global cases except Case II-low are considerably larger than that of the local simulation around the midplane. In particular, the high-resolution runs give quite large $\langle \frac{\delta \rho}{\rho} \rangle \approx 0.2$ around the midplane. Case II-high and Case II-high give similar $\langle \frac{\delta \rho}{\rho} \rangle$, although Case II-high gives smaller $\langle B^2 \rangle$ around the midplane (Figures 10 & 12). This implies that in Case II-high global effects such as the vertical differential rotation contribute to the density fluctuations in addition to the MRI. As will be examined by using a power spectrum in §5.2.3, the large value of $\langle \frac{\delta \rho}{\rho} \rangle$ in Case II-high comes from a large-scale structure. We infer that there is a connection between the vertical differential rotation and the large-scale density structure, which will be the subject of our future work.

In the context of the evolution of protoplanetary disks, such large density fluctuations greatly affect the dynamics of solid particles and subsequent planet formation (Nelson & Papaloizou 2004; Okuzumi & Ormel 2013; Ormel & Okuzumi 2013). Note, however, that nonisothermal local calculations show that the ratio of specific heats also affects $\frac{\delta\rho}{\rho}$ (Sano et al. 2004; Io & Suzuki 2014); realistic thermal physics is important in determining actual values of $\frac{\delta\rho}{\rho}$.

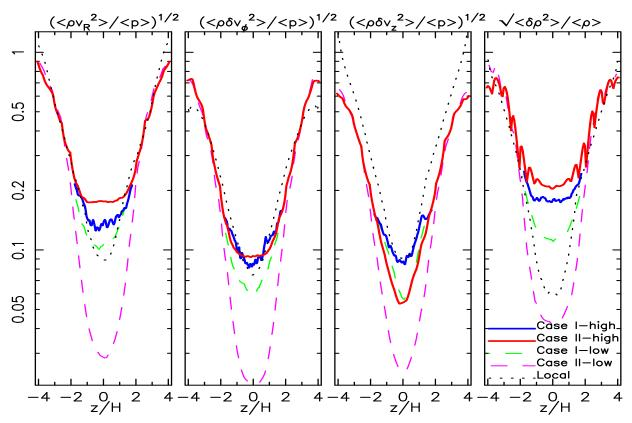


FIG. 19.— Vertical structures of velocity and density fluctuations of Case I-high (blue solid), Case II-high (red solid), Case II-low (green dashed), and Case II-high (magenta dashed) at $R=r_1(=5r_{\rm in})$. For comparison, the result of the local shearing box simulation is also shown (black dotted). From left to right are shown $\sqrt{\langle v_R^2 \rangle_{t,\phi}(r_1,z)/c_s}$, $\sqrt{\langle \delta v_\phi^2 \rangle_{t,\phi}(r_1,z)/c_s}$, $\sqrt{\langle \delta v_z^2 \rangle_{t,\phi}(r_1,z)/c_s}$, and $\langle \delta \rho/\rho \rangle_{t,\phi}(r_1,z)$ (See Equations 54 & 56).

5.2.2. Radial Profile

We examine the radial dependences of the velocity and density fluctuations by using Equation (27). The averages are taken with density weighted for the velocity fluctuations,

$$\frac{\sqrt{\langle \delta v_i^2 \rangle_{t,\phi,z}(R)}}{c_s} \equiv \sqrt{\frac{\langle \rho \delta v_i^2 \rangle_{t,\phi,z}(R)}{\langle p \rangle_{t,\phi,z}(R)}}, \tag{57}$$

and with the subtraction from the time- and ϕ -averaged quantity for the density fluctuations,

$$\langle \frac{\delta \rho}{\rho} \rangle_{t,\phi,z}(R) \equiv \sqrt{\frac{\langle (\rho(t,R,\phi,z) - \langle \rho \rangle_{t,\phi}(R,z))^2 \rangle_{t,\phi,z}(R)}{(\langle \rho \rangle_{t,\phi,z}(R))^2}},$$
(58)

in a manner similar to that for the vertical profiles (Equations 54 & 56). Figure 20 compares the fluctuations of velocity and density of Case I-high (left panel) and Case II-high (right panel). In Case II-high, we only show the values averaged in the midplane region, $\Delta z_{\rm mid}$ (Equation 28). In Case II-high, we also plot the values averaged in the surface regions over $\Delta z_{\rm sfc}$, Equation (29). Since Case II covers the vertical box from $z_{\rm bot} = -4H$ to $z_{\rm top} = 4H$, the integration over $\Delta z_{\rm sfc}$ corresponds to the sum of the integrations in the top and bottom surface regions between $\pm 3H$ and $\pm 4H$.

Both cases show similar values of the velocity fluctuations in $R \lesssim 8r_{\rm in}$; $\sqrt{\langle \delta v^2 \rangle}/c_{\rm s} \approx 0.1 - 0.2$, with values

mostly dominated by the R component. These values are slightly larger than a typical value, ≈ 0.1 , obtained in global simulations without a net vertical flux (Flock et al. 2011). The difference might imply the importance of the net vertical field in the velocity fluctuations. In $R \gtrsim 10r_{\rm in}$ in Case II-high, the velocity fluctuations decline to < 0.1 because the turbulence is still developing there. On the other hand, in $R \gtrsim 8r_{\rm in}$ in Case I-high, the velocity fluctuations increase. This trend is quite similar to that of $\frac{\langle B_R^2 \rangle_{t,\phi,z_{\rm tot}}}{\langle B_\phi^2 \rangle_{t,\phi,z_{\rm tot}}}$ in Figure 15, which is a good indicator for measuring the role of MRI in turbulence (Hawley et al. 2011).

Both Cases I-high and II-high give quite large density fluctuations, $\langle \delta \rho/\rho \rangle_{t,\phi,z_{\rm mid}}(R) \approx 0.2$ in the midplane region (see also Figure 19 for the vertical structure). In particular, Case II-high shows wavy structure of $\langle \delta \rho/\rho \rangle_{t,\phi,z_{\rm mid}}(R)$, which is anticorrelated with $\sqrt{\langle \delta v_\phi^2 \rangle_{t,\phi,z_{\rm mid}}(R)}/c_{\rm s}$. Compared with the bottom panel of Figure 15, the wavy pattern is well correlated with $-2\langle B_R B_\phi \rangle_{t,\phi,z_{\rm tot}}/\langle B^2 \rangle_{t,\phi,z_{\rm tot}}$ (Maxwell stress to magnetic pressure), which is a good indicator for MRI turbulence (Hawley et al. 2011). In other words, the density perturbations are more strongly excited in the regions with higher activities of MRI turbulence. An interesting thing is that these regions remain for a rather long time during $\Delta t_{\rm ave} = 600$ inner rotations or 55 local rotations at $R = 5r_{\rm in}$ in Case II-high, which might be related to zonal flows observed in local simulations (Johansen et al.

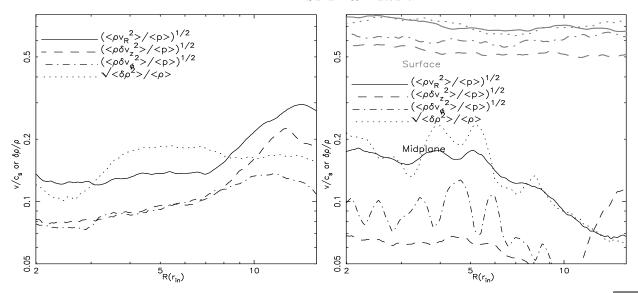


FIG. 20.— Radial structures of the velocity and density perturbations of Case I-high (left) and Case II-high (right). $\sqrt{\langle v_R^2 \rangle_{t,\phi,z}(r_1)/c_s}$ (solid), $\sqrt{\langle \delta v_\phi^2 \rangle_{t,\phi,z}(r_1)/c_s}$ (dashed), $\sqrt{\langle \delta v_z^2 \rangle_{t,\phi,z}(r_1)/c_s}$ (dot-dashed), and $\langle \delta \rho/\rho \rangle_{t,\phi,z}(r_1)$ (dotted) are plotted together in each panel. For Case II-high (right) the fluctuations integrated in the surface regions, $\Delta z_{\rm sfc}$ (Equation 29), are shown (thick gray), in addition to those integrated around the midplane, $\Delta z_{\rm mid}$ (black). In Case I-high the only data of the midplane integration are shown.

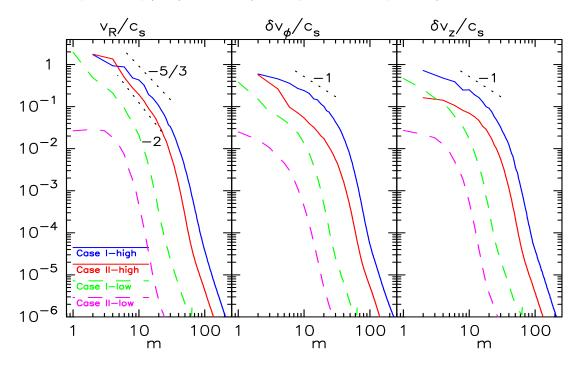


FIG. 21.— Azimuthal power spectra of nondimensional velocity fields, $\delta v_i/c_{\rm s}$, around the midplane of Case I-high (blue solid), Case II-high (red solid), Case II-low (green dashed), and Case II-low (magenta dashed). From left to right, the R, ϕ , and z components are displayed. The data are averaged over $\Delta z_{\rm mid}$, $\Delta R = r_1 \Rightarrow r_2$, and $\Delta t_{\rm ave}$. The low resolution runs (Cases II-low & II-low) cover m = 1-64, and the high resolution runs (Cases II-low & II-high) cover m = 2-256.

2009).

5.2.3. Azimuthal Power Spectra

We inspect azimuthal power spectra of velocity and density perturbations in a manner similar to inspection of the magnetic fields in §5.1.3. Figure 21 presents each component of the velocity power spectra. After taking the Fourier transformation of $\delta v_i/c_s$ ($i=R,z,\phi$) by Equation (30), the power spectra are derived from

Equation (31) by averaging over $\Delta z_{\rm mid}$ ($\pm H$ around the midplane; Equation 28), $\Delta R = r_1 \Rightarrow r_2$, and $\Delta t_{\rm ave}$. Here the fluctuation component is derived in the same way as in the analyses in real space (§5.2.1 & 5.2.2), $\delta v_i = (v_R, \delta v_\phi, \delta v_z)$, by using Equations (49) & (55). The azimuthal mode is covered from $m_l = 1$ to $m_h = 64$ in the low-resolution runs, and from $m_l = 2$ to $m_h = 256$ in the high-resolution runs.

Figure 21 presents the derived power spectra of the

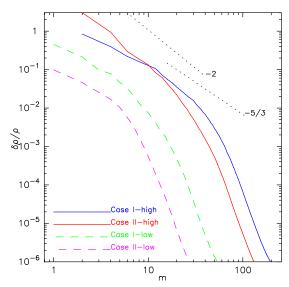


FIG. 22.— Azimuthal power spectra of density perturbations, $\delta \rho/\rho$, around the midplane of Case I-high (blue solid), Case II-high (red solid), Case II-low (green dashed), and Case II-low (magenta dashed). The data are averaged over $\Delta z_{\rm mid}$, $\Delta R = r_1 \Rightarrow r_2$, and $\Delta t_{\rm ave}$. The low resolution runs (Cases I-low & II-low) cover m=1-64, and the high resolution runs (Cases II-low & II-high) cover m=2-256.

velocity perturbations. Compared to the power spectra of the magnetic fields (Figure 18), all the cases except for Case II-low exhibit steeper slopes. The R component of the high-resolution runs gives the spectra, $\propto m^{-5/3}-m^{-2}$. Here, $m^{-5/3}$ is the Kolmogorov scaling derived from incompressible hydrodynamical turbulence (Kolmogorov 1941), and m^{-2} corresponds to the Burgers (1939)' type shock dominated spectrum.

Figure 22 displays the power spectra of the density perturbations. The obtained slopes are roughly similar to those for v_R/c_s . An interesting feature is that in Case II-high the lowest m=2 mode largely dominates higher m modes, compared to Case I-high. This implies the existence of a non-axisymmetric but small-m (large-scale) zonal structure with a density bump or dip for a rather long time, $\sim \Delta t_{\rm ave}$ in Case II-high.

5.3. Vertical Outflows & Wave Phenomena

Suzuki & Inutsuka (2009) & Suzuki et al. (2010) pointed out MRI turbulence in accretion disks could play a role in driving disk winds particularly in mass loading to the surface regions. Such vertical outflows were also reported by 2D axisymmetric global simulations (Stone & Pringle 2001; Proga & Begelman 2003; Mościbrodzka & Proga 2009). Recently, various aspects of relations between MRI turbulence and disk winds have been studied by both local simulations (Bai & Stone 2013a,b; Fromang et al. 2013; Lesur et al. 2013) and global simulations (Flock et al. 2011). In addition to MRI, Parker instability is also studied as a reliable mechanism in driving vertical outflows (Nishikori et al. 2006; Machida et al. 2013).

The upper panel of Figure 23 shows that disk winds are also observed in our global simulations. In Case I-high (solid) the disk winds are driven from the near-midplane regions, because the vertical extent of the simulation box is insufficient and only $\pm 1.8H$ at $R = r_1 (= 5r_{\rm in})$. As discussed in Suzuki et al. (2010) and Fromang et al. (2013)

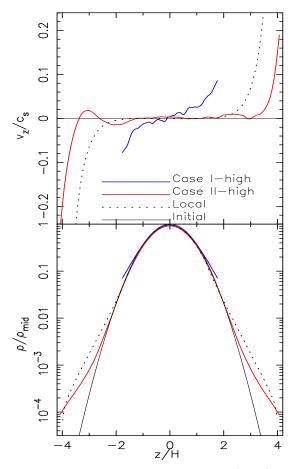


Fig. 23.— Comparison of vertical velocities (upper) and densities (lower) of Case I-high (blue solid) at $R=r_1(=5R)$, Case II-high (red solid) at $R=r_1$, the local simulation (black dotted), and the initial condition (black solid) on z/H. v_z in the upper panel is normalized by the local sound speed, and ρ in the lower panel is normalized by the time and ϕ averaged density at the midplane.

by using local shearing boxes, the mass flux of the disk winds depends on the vertical box size; a smaller vertical size gives a larger mass flux. The result of Case I-high is consistent with this trend.

Case II-high (dashed lines in Figure 23) has the same vertical box size $= \pm 4H$ as the local simulation. The onset positions of the disk winds in Case II-high are located at slightly higher altitudes than those of the local simulation. A reason for the difference is related to the intermittent natures of MRI-driven disk winds. In the local simulations (Suzuki & Inutsuka 2009; Suzuki et al. 2010), we observed quasi-periodicity of the driving disk winds with 5-10 rotation times, caused by the breakups of channel-mode flows. In contrast, in Case IIhigh the intermittency is more random with time as in Figure 24, mainly because quasi-periodic channel flows seen in the local simulation are distorted by the vertical differential rotation. During the time integration, $\Delta t_{\rm ave} = 1200 - 1800$ inner rotations, the disk wind from the upper surface ceases for a while, which causes the slower onset of the disk wind from the upper surface in the time-averaged structure (upper panel of Figure 23). However, during strong wind phases, the wind speed at the surfaces far exceeds the sound speed (Figure 8) and the onset heights are comparable to that observed in the

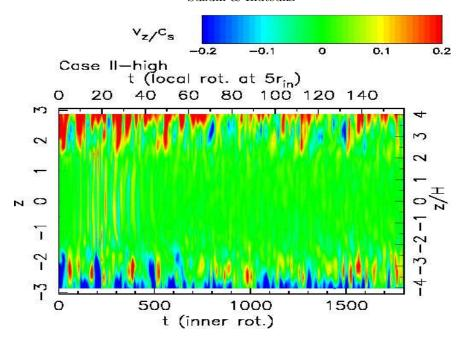


Fig. 24.— t-z diagrams of $\langle v_z \rangle_{\phi}(r_1, z)$ normalized by the sound speed at $R = r_1 (= 5r_{\rm in})$ for Case II-high. On the horizontal axis are shown time in units of the inner rotation (top of panel) and time in units of the local rotation at $r = r_1$ (bottom of panel). On the vertical axis are shown z (left to panel) and z/H (right to panel).

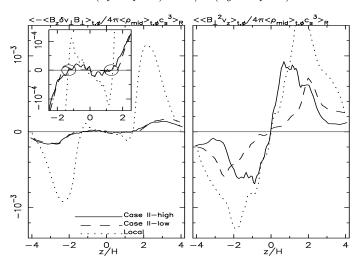


Fig. 25.— Comparison of the vertical structures of the Poynting flux associated with magnetic tension (left) and Poynting flux associated with the magnetic pressure and the advected magnetic energy (right) of Case II-high (solid), Case II-low (dashed), and the local simulation (dotted). Here the values of the global simulations are averaged from $R=r_1$ to r_2 in addition to the time and ϕ averaging. In the inset in the left panel a region around the midplane is zoomed in. The two circles at $z=\pm 1.3H$ indicate the injection regions of the tension-associated Poynting flux.

local simulation.

The bottom panel of Figure 23 shows that the gas is lifted up near the surface regions from the initial density distribution; the simulated density structures deviate from the initial profile around the onset locations of the disk winds.

In Suzuki & Inutsuka (2009), we claimed that the disk winds are driven by the Poynting flux associated with the MHD turbulence from the results of the local shearing box simulations. We also found that the Poynting flux of the magnetic tension is injected from $z\approx \pm 1.5 H$,

which we call "injection regions", toward the surfaces and the midplane because of the intermittent breakups of channel-mode flows. We inspect whether these characteristic features of the disk winds are also observed in the global simulations.

We can write the z component of energy flux as follows:

$$\rho v_z \left(\frac{1}{2} v^2 + h + \Phi \right) + v_z \frac{B_\perp^2}{4\pi} - \frac{B_z}{4\pi} (v_\perp B_\perp), \tag{59}$$

where $B_{\perp}^2 = B_R^2 + B_{\phi}^2$ and $v_{\perp}B_{\perp} = v_R B_R + v_{\phi} B_{\phi}$ (Suzuki & Inutsuka 2009). The last two terms originate from the Poynting flux; the first term is related to the sum of magnetic pressure and advected magnetic energy ⁷, and the second term is associated with magnetic tension. Here we pick up the fluctuation component of perpendicular velocity, $\delta v_{\perp} = (v_R, \delta v_{\phi})$, as in Equations (49). Then the fluctuation component of the Poynting flux with magnetic tension can be rewritten as

$$-\frac{1}{4\pi}B_z\delta v_{\perp}B_{\perp} = \rho v_{A,z}(\delta v_{\perp,+}^2 - \delta v_{\perp,-}^2),$$
 (60)

where $\delta v_{\perp}B_{\perp}=v_{R}B_{R}+\delta v_{\phi}B_{\phi}$, $v_{A,z}=B_{z}/\sqrt{4\pi\rho}$, and $\delta v_{\perp,\pm}=\frac{1}{2}(\delta v_{\perp}\mp B_{\perp}/\sqrt{4\pi\rho})$ are Elsässer variables, which correspond to the amplitudes of Alfvén waves propagating in the $\pm B_{z}$ directions.

Figure 25 compares the vertical structures of the Poynting flux. Since we would like to study the structures at high altitudes, we present the results of Cases II-high (solid lines) and II-low (dashed lines) in comparison with the result of the local simulation (dotted line), and we do not show the results of Cases I-high

 $^{^7}$ Here, the term $\frac{B_\perp^2}{4\pi}$ consists of work per time (i.e. power) done by magnetic pressure, $\frac{B_\perp^2}{8\pi}$ and magnetic energy, $\frac{B_\perp^2}{8\pi}$, advected with velocity, v_z

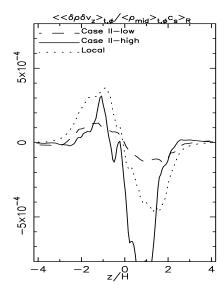


FIG. 26.— Comparison of the vertical structures of the normalized energy flux of sound waves of Case II-high (*solid*), Case II-low (*dashed*), and the local simulation (*dotted*).

and I-low, of which the vertical box sizes are |z| < 2H. What are shown here are the Poynting flux with magnetic tension, $\langle -\langle B_z \delta v_\perp B_\perp \rangle_{t,\phi}(z)/4\pi \langle \rho_{\rm mid} \rangle_{t,\phi} c_s^3 \rangle_R$ (left), and the Poynting flux of the sum of magnetic pressure and advected energy, $\langle \langle B_\perp^2 v_z \rangle_{t,\phi}(z)/4\pi \langle \rho_{\rm mid} \rangle_{t,\phi} c_s^3 \rangle_R$ (right panel), where we take the averages from $R=r_1$ to r_2 after normalizing by $\langle \rho_{\rm mid} \rangle_{t,\phi} c_s^3$ at the midplane, in addition to the usual averages over $\Delta t_{\rm ave}$ and ϕ (Equation 22).

Figure 25 shows that the global simulations (solid and dashed lines) give magnitudes for both components of the Poynting fluxes that are smaller than those of the local simulation (dotted line). Then, the mass fluxes of the disk winds in the global simulations are smaller than that of the local simulation. In the global simulations (solid and dashed lines) the Poynting fluxes with the magnetic tension $(-\langle B_z \delta v_\perp B_\perp \rangle/4\pi)$ give smaller contributions to the disk winds than the Poynting flux associated with the magnetic pressure and energy $(\langle B_\perp^2 v_z \rangle/4\pi)$, while in the local simulation (dotted lines) both components give comparable contributions.

Although the magnitudes are smaller, the Poynting fluxes with the magnetic tension in the global simulations show qualitative vertical structures similar to that of the local simulation; at $z\approx \pm 1.3H$ the solid and dashed lines cross x=0, indicated by the circles in the left panel of Figure 25. This indicates that from these regions the Poynting fluxes with the magnetic tension are injected in both directions.

In Suzuki & Inutsuka (2009) we also found sound waves traveling from the surface regions to the midplane, which is related to the injection regions of the Poynting flux with the magnetic tension. The energy flux of sound waves in static media is expressed as

$$\delta\rho\delta v_z c_s^2 = \rho c_s (\delta v_{\parallel,+}^2 - \delta v_{\parallel,-}^2), \tag{61}$$

where $\delta \rho = \rho - \langle \rho \rangle_{t,\phi}$, $\delta v_z = v_z - \langle \rho v_z \rangle_{t,\phi} / \langle \rho \rangle_{t,\phi}$ (Equation 55), and $\delta v_{\parallel,\pm} = \frac{1}{2} \left(\delta v_z \pm c_s \frac{\delta \rho}{\rho} \right)$ are

the amplitudes of sound waves propagating in the $\pm z$ directions. Figure 26 compares the energy flux of sound waves, $\langle\langle\delta\rho\delta v_z\rangle_{t,\phi}(z)c_{\rm s}^2\rangle\langle\langle\rho_{\rm mid}\rangle_{t,\phi}c_{\rm s}^3\rangle_R = \langle\langle\delta\rho\delta v_z\rangle_{t,\phi}(z)/\langle\rho_{\rm mid}\rangle_{t,\phi}c_{\rm s}\rangle_R$, where the average and normalization are taken in the same manner as for the Poynting flux. The global simulations show that the sound waves are directed toward the midplane from the surface regions, which is consistent with the trend obtained in the local simulations. The sound waves themselves carry mass flux $(\delta\rho\delta v_z)$, and the direction (to the midplane) is opposite the direction (to the surfaces) of the mass flux carried by the disk winds. In protoplanetary disks, these sound waves possibly play a role in the dynamics of solid materials (Suzuki & Inutsuka 2009; Okuzumi & Hirose 2011, 2012).

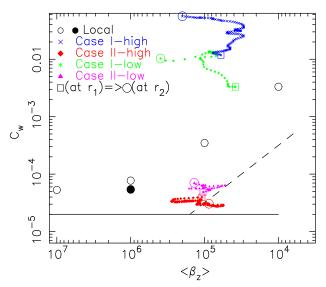


FIG. 27.— Dependence of normalized mass flux, $C_{\rm w}$, of the disk winds on plasma $\langle \beta_z \rangle_{t,\phi,z_{\rm tot}}$ for net vertical magnetic fields in $r_1 < R < r_2$. Multiple data points for each case of the global simulations correspond to different radial locations. Colored squares and circles indicate the data at $R=r_1$ and $R=r_2$ of each case. Case I-high (blue crosses), Case II-high (red diamonds), Case I-low (green asterisks), and Case II-low (magenta triangles) are compared with the local simulations by Suzuki et al. (2010, jopen circles for low-resolution runs and filled circle for high-resolution run). The solid line is a 'floor' value based on the local simulations and the dashed line is a fit for the increasing trend of $\langle C_{\rm w} \rangle$ (Suzuki et al. 2010).

Before concluding this subsection, we examine the dependence of the mass flux of the disk winds on the net vertical magnetic field strength. Figure 27 presents the sum of the nondimensional mass fluxes of the disk winds from the top (subscript "top") and bottom (subscript "bot") surfaces,

$$\langle C_{\rm w} \rangle_{t,\phi}(R) = \frac{\langle (\rho v_z)_{\rm top} - (\rho v_z)_{\rm bot} \rangle_{t,\phi}}{\langle \rho_{\rm mid} \rangle_{t,\phi} c_{\rm s}},$$
 (62)

as a function of $\langle \beta_z \rangle_{t,\phi,z_{\rm tot}}(R)$ (Equation 52), corresponding to (the inverse of) the net vertical field strength. Note that the negative sign for $(\rho v_z)_{\rm bot}$ is because $v_z < 0$ corresponds to an outflow from the bottom surface.

Cases I-high and I-low give systematically larger $\langle C_{\rm w} \rangle$ because the vertical box size in units of scale height in these cases is smaller ($\pm 1.8 H$ at $R=r_1$ and $\pm 1.3 H$ at $R=r_2$) and the gas streams out rapidly, as shown in Figure 23. Since this is an unphysical reason, we

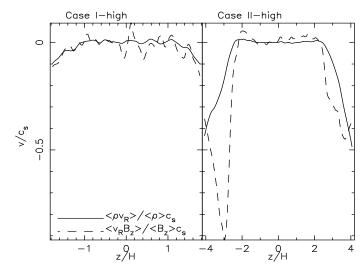


FIG. 28.— Vertical structure of time and ϕ averaged radial velocity at $R=r_1(=5r_{\rm in})$ normalized by the local sound speed of the gas (solid; Equation 63) and the vertical magnetic field (dashed; Equation 64) of Case I-high (left) and Case II-high (right).

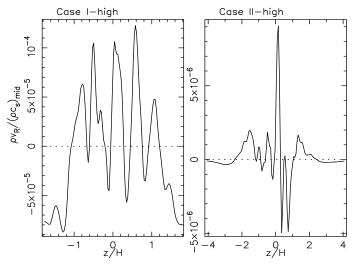


FIG. 29.— Vertical structure of time and ϕ averaged radial mass flux, ρv_R , at $R=r_1(=5r_{\rm in})$ normalized by the local sound speed multiplied by the density at the midplane, $(\rho c_{\rm s})_{\rm mid}$, (solid) of Case II-high (left) and Case II-high (right). The zero level is shown by the dotted line.

mainly discuss the results of Cases II-high and II-low here. Contrary to the $\langle \alpha \rangle_{t,\phi,z_{\rm tot}}(R)$ values (Figure 17), the mass flux shows almost no dependence on the resolution; the lower-resolution case (Case II-low; magenta triangles) rather gives slightly higher $\langle C_{\rm w} \rangle$. This is because the disk winds are driven from the surface regions where both the low-resolution and high-resolution runs give the comparable magnetic field strengths (Figure 10). Compared to the local simulation, Cases II-high and II-low give smaller $\langle C_{\rm w} \rangle$ because of the more random time dependency discussed in Figure 23.

5.4. Radial Flows

In this subsection, we inspect the radial motions of the gas and the vertical magnetic field of the simulated accretion disks. Figure 28 presents the vertical structures of the radial velocities of Case I-high (*left*) and Case IIhigh (*right*). We derive the radial velocity of the gas

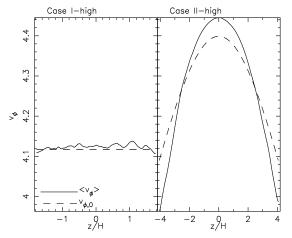


Fig. 30.— Vertical structure of time and ϕ averaged azimuthal velocity at $R = r_1(5r_{\rm in})$ (solid; Equation 65) of Case I-high (left) and Case II-high (right) in comparison with the initial value (dashed).

by density-weighted average over time, Δt_{ave} , and ϕ at $R = r_1 (= 5r_{\text{in}})$,

$$\langle \frac{v_{R,\text{gas}}}{c_{\text{s}}} \rangle_{t,\phi}(r_1, z) = \frac{\langle \rho v_R \rangle_{t,\phi}(r_1, z)}{\langle \rho \rangle_{t,\phi}(r_1, z) c_{\text{s}}}.$$
 (63)

As for the movement of the vertical magnetic field, we adopt a similar averaging procedure:

$$\langle \frac{v_{R,B_z}}{c_s} \rangle_{t,\phi}(r_1,z) = \frac{\langle B_z v_R \rangle_{t,\phi}(r_1,z)}{\langle B_z \rangle_{t,\phi}(r_1,z)c_s}.$$
 (64)

Both Cases I-high and II-high show that the mass accretions (solid lines) take place near the surfaces, while in the midplane regions the radial velocities are quite small with the averages being slightly positive with fluctuations. This is because the Maxwell stresses $(-\langle B_R B_\phi \rangle/4\pi \langle p \rangle)$ are larger in the surface regions (Figure 12), and the outward transport of the angular momentum is more effective there.

To see the mass flows, we plot the vertical structure of $\langle \rho v_R \rangle_{t,\phi}(r_1,z)$ normalized by $[\langle \rho \rangle_{t,\phi}(r_1)c_s]_{\rm mid}$ at the midplane in Figure 29. As expected, one can observe accretion in the surface regions and fluctuating outward and inward mass flows near the midplane in both Cases I-high (left panel) and II-high (right panel). In Case I-high the accretion in the surface regions dominates and the vertically integrated mass flux, $\int dz \langle \rho v_R \rangle_{t,\phi}(r_1,z)$, is directed inward. On the other hand, in Case II-high the magnitude of the mass flux near the surfaces is small because of the low density and is dominated by the outward mass flows in 1 < |z/H| < 2. Thus the direction of the vertically integrated mass flux is outward.

The radial velocities of the vertical magnetic fields roughly follow the trend of the gas flows in both cases. However, $\langle \frac{v_{R,\mathrm{gas}}}{c_{\mathrm{s}}} \rangle$ and $\langle \frac{v_{R,B_z}}{c_{\mathrm{s}}} \rangle$ do not exactly follow each other, which means that the gas and the vertical magnetic flux are not exactly frozen-in because of magnetic reconnections. Since our numerical code adopts the ideal MHD equations, this is purely a numerical effect; magnetic reconnections occurs because of small-scale turbulent fields in the sub-grid scales.

What we observe in the simulations is similar to the layered accretion which is proposed for the evolution of protoplanetary disks (Gammie 1996). In that scenario,

the accretion is inhibited around the midplane because a so-called dead zone, which is an inactive region with respect to MRI due to insufficient ionization, forms there. On the other hand, the layered accretion obtained in our simulations occurs simply because of the vertical structure of the α stress. Figure 30 compares the time- and ϕ -averaged vertical structure of density-weighted azimuthal velocity (solid line),

$$\langle v_{\phi} \rangle_{t,\phi}(r_1, z) = \frac{\langle \rho v_{\phi} \rangle_{t,\phi}(r_1, z)}{\langle \rho \rangle_{t,\phi}(r_1, z)},\tag{65}$$

with the initial value (dashed line). In Case II-high (right panel), the rotation speed becomes slower in the surface regions than the initial state because a larger angular momentum is extracted there as a result of the larger α stress. This further leads to the layered accretion discussed so far.

Takeuchi & Lin (2002) also derived a similar vertical profile for the layered radial velocity of the gas, mainly because of the vertical differential rotation, which is considered in our Case II. Takeuchi & Lin (2002) as well as Keller & Gail (2004) and Jacquet (2013) apply this radial velocity profile to the outward migration of dust particles, which is consistent with observed crystalline solid particles in the outer regions of protoplanetary disks (Bouwman et al. 2008). Our simulations also support the radial outward flows at the midplane.

The vertical variation of radial flows also triggers instability even in the hydrodynamical gas without magnetic field (Goldreich & Schubert 1967; Fricke 1968; Nelson et al. 2013). We need further studies to determine whether this type of instability is effective in the presence of vertical magnetic flux.

The layered accretion we observe is totally opposite to a trend obtained in simulations without a net vertical magnetic flux (Fromang et al. 2011; Flock et al. 2011); in their simulations, the gas moves outwardly in the surface regions. This might indicate the importance of vertical magnetic fields in detailed properties of mass accretion. However, we should be careful, because the layered accretion obtained in our simulations might be due to the boundary condition at the disk surfaces, $\theta = \theta_{\rm max} \& \theta_{\rm min}$. Since our simulations handle the net vertical magnetic fields in the spherical coordinates, we need to take special care at the boundaries, which we discuss further later in this subsection.

Transport of angular momentum is a key to control radial flows in accretions disks (e.g., Lynden-Bell & Pringle 1974). In order to quantitatively study the mechanisms that drive the radial flows, we examine the transport of the angular momentum in the simulated disks. For our analyses, we begin with an equation for the conservation of momentum in the ϕ direction (i.e. conservation of angular momentum) in the cylindrical coordinates. Since we take the ϕ averages, we start from an axisymmetric equation:

$$\frac{\partial}{\partial t}(\rho R v_R) + \frac{1}{R} \frac{\partial}{\partial R} \left[R^2 \left(\rho v_R v_\phi - \frac{B_R B_\phi}{4\pi} \right) \right]
+ \frac{\partial}{\partial z} \left[R \left(\rho v_R v_z - \frac{B_R B_z}{4\pi} \right) \right] = 0.$$
(66)

Taking the integration from $z=z_{\rm bot}$ to $z=z_{\rm top},$ we have

$$R^{2}\Omega \frac{\partial \Sigma}{\partial t} + R \frac{\partial}{\partial t} (\Sigma \delta v_{\phi}) + \frac{1}{R} \frac{\partial}{\partial R} (R^{3}\Sigma \Omega v_{R} + R^{2}\Sigma w_{R\phi}) + \left[\rho R^{2}\Omega v_{z} + R \left(\rho \delta v_{\phi} v_{z} - \frac{B\phi B_{z}}{4\pi} \right) \right]_{z_{\text{bot}}}^{z_{\text{top}}} = 0, \quad (67)$$

where $\Omega = v_{\phi}/R$ is rotation frequency and

$$\Sigma w_{R\phi} \equiv \int_{z_{\text{bot}}}^{z_{\text{top}}} dz \left(\rho v_R v_\phi - \frac{B_R B_\phi}{4\pi} \right) \tag{68}$$

is α multiplied by p and integrated with z. The last term of Equation (67) indicates the loss of angular momentum by the disk winds from the top ($z = z_{\text{top}}$) and the bottom ($z = z_{\text{bot}}$) of a simulation box.

In order to rearrange Equation (67) to a more useful form, we use an equation for the mass conservation,

$$\frac{\partial \rho}{\partial t} + \frac{1}{R} \frac{\partial}{\partial R} (\rho v_R R) + \frac{\partial}{\partial z} (\rho v_z) = 0.$$
 (69)

As we did for Equation (66), we integrate Equation (69) from $z = z_{\text{bot}}$ to $z = z_{\text{top}}$ to have

$$R^{2}\Omega \frac{\partial \Sigma}{\partial t} + R\Omega \frac{\partial}{\partial R} (\Sigma v_{R}R) + R^{2}\Omega [\rho v_{z}]_{z_{\text{bot}}}^{z_{\text{top}}} = 0$$
 (70)

Combining Equations (67) and (70), we can derive an equation that determines radial velocity as

$$v_{R,\text{ang}} = \left[-R \frac{\partial}{\partial t} (\Sigma \delta v_{\phi}) - \frac{1}{R} \frac{\partial}{\partial R} (R^{2} \Sigma w_{R\phi}) - \left\{ R \left(\rho \delta v_{\phi} v_{z} - \frac{B_{\phi} B_{z}}{4\pi} \right) \right\}_{z_{\text{bot}}}^{z_{\text{top}}} \right] \left[\Sigma \frac{\partial}{\partial R} (R^{2} \Omega) \right]^{-1},$$
(71)

where we use the subscript "ang" to explicitly show that this v_R is estimated from the balance of angular momentum, and the physical meaning of each term in the numerator would be clear. The second and third terms denote the change of angular momentum by magnetoturbulent stresses and disk winds respectively. The first term arises from the change of mass distribution with time.

Figure 31 presents the mass accretion rates,

$$\dot{M}_R(R) = 2\pi R \int_{z_{\text{bot}}}^{z_{\text{top}}} dz \rho v_R \tag{72}$$

of Case I-high (left panel) and II-high (right panel) and the contributions from each term in Equation (71), where we use \dot{M}_R in the cylindrical coordinates instead of \dot{M}_r (Equation 36). Note that $\dot{M}_R < 0$ corresponds to accretion and $\dot{M}_R > 0$ corresponds to radial outflows. The red lines are the measured mass accretion rates from the simulations and the black lines are the estimated accretion rates using $v_{R,\rm ang}$ of Equation (71),

$$\dot{M}_{R,\rm ang} = 2\pi R \Sigma v_{R,\rm ang}.$$
 (73)

In the figure, the breakdown of the three contributions to the accretion rate is also shown. The contribution from the turbulent stress (dashed lines) is calculated by using the only 2nd term of Equation (71) when deriving $v_{R,\rm ang}$.

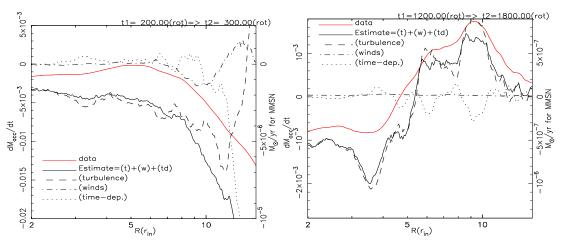


Fig. 31.— Comparison of the mass accretion rates of Case I-high (*left*) and Case II-high (*right*). In each panel, the measured accretion rate (*red solid*; Equation 72) is compared with the accretion rate estimated from the transport of the angular momentum, Equation (73; *black solid*). The other three lines are the breakdown of the estimated accretion rate; the dashed line corresponds to the mass accretion driven by the turbulent stress, the dot-dashed line is that by the disk winds, and the dotted line is the contribution from the time-dependent term in Equation (71).

The contributions from the disk winds (dot-dashed lines) and the time-dependent term (dotted lines) can be derived in the same manner.

Figure 31 shows that the estimated accretion rates $(M_{R,ang}; black solid lines)$ explain the overall trends of the measured accretion rates $(M_R; \text{ red solid lines}),$ whereas the deviations of \dot{M}_R from $\dot{M}_{R,\rm ang}$ are not small because of the truncation errors when converting from the spherical coordinates used in the simulations to the cylindrical coordinates, which are further accumulated during the long time integration. In both the cases, the radial mass flows are mainly determined by the turbulent stress (dashed lines). The time-dependent term also gives significant contributions in some regions, which indicates that the assumption of the steady state is not good for the simulated disks. The contribution from the disk winds (dotted lines) is much smaller than the other two components. Although in the outer region $(R > 15r_{\rm in})$ of Case I-high the disk winds become significant, the effect of the disk winds is overestimated in this region because the simulation box can cover up to only $z \approx \pm H$ in Case I-high.

While in Case I-high the mass is accreting ($\dot{M}_R < 0$) in the entire region, in Case II-high the mass is going outward ($\dot{M}_R > 0$) in $R > 5r_{\rm in}$. This radially outward flow is natural during the evolution of accretion disks (e.g., Lynden-Bell & Pringle 1974). In this region of Case II-high, the angular momentum supplied from the inner region is larger than the angular momentum lost to the outer region. The net angular momentum increases in a ring located in $R > 5r_{\rm in}$, and then the gas moves outward.

Figure 32 displays radial dependences of the motion of the vertical magnetic field,

$$\langle \frac{v_{R,B_z}}{c_s} \rangle_{t,\phi,z} = \frac{\langle B_z v_R \rangle_{t,\phi,z}(R)}{\langle B_z \rangle_{t,\phi,z}(R) c_s},$$
 (74)

in comparison with the radial velocity of the gas,

$$\langle \frac{v_{R,\text{gas}}}{c_{\text{s}}} \rangle_{t,\phi,z} = \frac{\langle \rho v_R \rangle_{t,\phi,z}(R)}{\langle \rho \rangle_{t,\phi,z}(R) c_{\text{s}}}.$$
 (75)

For the radial velocity of B_z in Equation (74) we take the average in the midplane region, $\Delta z_{\rm mid}$ (Equation 28), and in the surface regions, $\Delta z_{\rm sfc}$ (Equation 29), to compare the motions of the vertical magnetic flux at the midplane and in the surface regions. For the radial flow of gas in Equation (75), we average v_R over the entire surface $\Delta z_{\rm tot}$ (Equation 26) to see the net gas flow. As shown in Figures 28 & 31, the radial velocities could be either positive or negative. In order to display both positive and negative values in the logarithmic scale, we take the absolute values and use dashed lines for radially inward flows ($v_R < 0$) and solid lines for radially outward flows ($v_R > 0$).

In both Cases I-high (left panel in Figure 32) and IIhigh (right panel), the motions of the net $\langle B_z \rangle$ near the midplane and in the surface regions are very different. In the surface regions, the vertical magnetic flux mostly moves inward at a quite high speed, $\gtrsim 0.1c_{\rm s}$. On the other hand, at the midplane, no clear tendencies are observed in either case; $\langle B_z \rangle$ moves outward in some regions and inward in other regions at slow speeds, $\lesssim 0.01c_{\rm s}$. (Note that in the outer region of Case I-high, v_R/c_s becomes large because of the effect of the surface boundaries.) These different properties of the net $\langle B_z \rangle$ indicate that the vertical magnetic field lines are not connected from the midplane to the surface regions when considering the long time integration, Δt_{ave} . The inward dragged magnetic field lines in the surface regions continuously reconnect with field lines in the midplane region because of the numerical resistivity; although our simulations assume the ideal MHD, magnetic reconnections could take place in the sub-grid scales as a result of the numerical diffusion. For the same reason, the motions of the vertical magnetic fields are also not strictly coupled to the motions of the gas.

As shown so far, our simulations show the inward dragging of the vertical magnetic flux in the surface regions, which follows the trend of the layered accretion of the gas component. Interestingly enough, this is consistent with a recent result based on an analytic model (Rothstein & Lovelace 2008), while different trends could be realized with different settings (Lubow et al. 1994). The

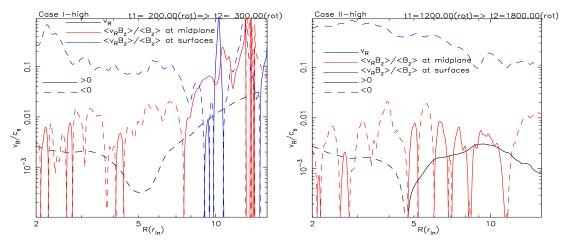


Fig. 32.— Comparison of radial velocities of the gas (black), and the net vertical fields in the midplane region (red) and in the surface regions (blue) of Case I-high (left) and Case II-high (right). Dashed lines correspond to inward velocities, $v_R < 0$, and solid lines indicate outward velocities, $v_R > 0$.

inward advection of B_z in the surface regions will cause a concentration of the magnetic flux around a central object, which is suitable for driving strong jets (Beckwith et al. 2009). However, we should carefully state that this trend might be affected by the boundary condition at the disk surfaces. Our simulations adopt the outgoing condition based on a characteristic method (Suzuki & Inutsuka 2006) at the surface boundaries (see §2.2). Thus, no information comes into the simulation box. However, in realistic situations, a global magnetic field is probably anchored in somewhere above a disk, e.g. in coronal regions above the disk surfaces (e.g., Kato et al. 2004; Ohsuga et al. 2009; Beckwith et al. 2009). In this case, the inward advection of the vertical magnetic flux observed in our simulations would eventually be stopped as well as further wound up by the vertical differential rotation. Later on, the configuration of the global magnetic field would be suitable for magneto-centrifugal driven winds (Blandford & Payne 1982; Kudoh et al. 1998), which also contributes to the transport of the angular momentum of the disk. For simulations in more realistic situations, we need a larger simulation box particularly in the θ direction, although it is a trade-off for the numerical resolution in a disk region.

5.5. Toroidal B field

Temporal oscillations of toroidal magnetic fields are a universal phenomenon in MRI-induced accretion disks (e.g., Davis et al. 2010; Flock et al. 2011). Our global simulations show similar trends as illustrated in Figure 33 which displays the t-z diagrams of $\langle B_\phi \rangle_\phi(r_1,z)$. Cases II-high and II-low show more distinctive oscillating features than Cases I-high and I-low because Cases II-high and II-low cover the larger vertical region measured in scale height. This indicates that the magnetic fields at high altitudes $(z\gtrsim 2H)$ are important in the flip-flops of the toroidal magnetic fields.

Compared to results of local simulations (e.g., Davis et al. 2010), the quasi-periodic nature of oscillatory features is deformed in our global simulations, in a manner similar to the time-dependent properties of the disk winds (Figure 24 in §5.3). The four cases show that in the upper hemisphere $(z > 0) \langle B_{\phi} \rangle$ tends to be positive (redder colors), while in the lower hemisphere (z < 0)

 $\langle B_\phi \rangle$ tends to be negative (bluer colors). This is related to the layered advection of the vertical magnetic fields discussed in §5.4. $\langle B_z \rangle$ is advected inward in the surface regions. Focusing on a single field line, it rotates faster in the surface regions as a consequence of this inward advection. Thus, positive (negative) $\langle B_\phi \rangle$ is created near the upper (lower) surface. However, this might be affected by the boundary condition at the surfaces as discussed in §5.4. If a global poloidal magnetic field is anchored in coronal regions which are outside the simulation box, the layered advection of the vertical field lines would eventually be inhibited and the systematic generation of $\langle B_\phi \rangle$ would also be suppressed.

6. DISCUSSION

6.1. Entire Region of Case II

In Case II we use the very large radial extent ($\sim 500r_{\rm in}$) of the simulation box (Table 1). However, since our purpose is to study the saturated state of the magnetic field, we have focused on the region in $r \leq 10r_{\rm in}$ so far; in the outer region, the magnetic field is still in the growth phase. Here, we briefly introduce the evolution of the magnetic field in the entire radial extent of Case II-high. Figure 34 presents the evolution of the magnetic energy at different heights, z=0 (upper panel) and z=3H (lower panel), normalized by the gas pressure at the midplane,

$$\frac{\langle B^2 \rangle_{\phi}(t, r, z)}{8\pi \langle p_{\text{mid}} \rangle_{\phi}(t, r)} \tag{76}$$

in the time (horizontal axis) – r (vertical axis) diagram. Both panels show that the amplification of the magnetic fields proceeds with time in proportion to the Keplerian rotation time, $t \propto r^{3/2}$. At the midplane the magnetic field is mainly amplified by the MRI. In the surface region, the growth of the magnetic field is roughly ten times faster, which is triggered by the vertical differential rotation.

6.2. Implication for Observation of Spirals in Protoplanetary Disks

In Figure 7 in §4.1 we showed spiral structures in the face-on views of $\log(1/\beta)$. Although the disks are tur-

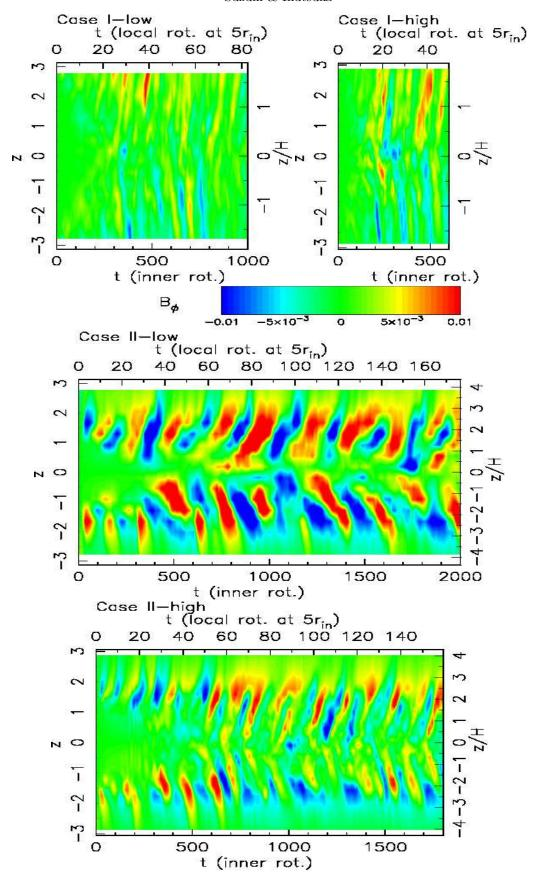


Fig. 33.— t-z diagrams of $\langle B_{\phi} \rangle_{\phi}(r_1,z)$ at $R=r_1(=5r_{\rm in})$ for Case I-low (top-left), Case I-high (top-right), Case II-low (Middle), and Case II-high (Bottom). On the horizontal axis are shown time in units of the inner rotation (top of panels) and time in units of the local rotation at $r=r_1$ (bottom of panels). On the vertical axis are shown z (left to panels) and z/H (right to panels).

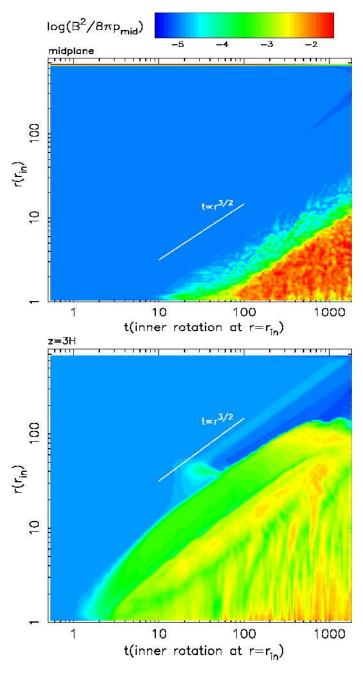


FIG. 34.— t—r diagrams of the magnetic energy normalized by the gas pressure at the midplane, $\langle B^2 \rangle_\phi(t,z,r)/8\pi \langle p_{\rm mid} \rangle_\phi(t,z,r)$, at z=0 (midplane; upper) and at z=3H (lower) of Case II-high. Both axes are in logarithmic scale. The white line shows the relation of the Keplerian rotation time, $t \propto r^{3/2}$.

bulent, pressure balance is supposed to be roughly satisfied between high- β (weak B) region and low- β (strong B) regions, where high- β regions correspond to denser regions. Applying the result of Figure 7 to protoplanetary disks, denser high- β regions are expected to have a larger number of dust grains than lower- β regions. Thus, similar spiral structures are expected to be seen in scattered-light observations, e.g., in the near-infrared wavelength. Recent near-infrared observations of protoplanetary disks found many remarkable spiral structures. Many authors tend to interpret those structures

as being caused by unseen planets embedded in the disks (e.g., Hashimoto et al. 2011; Muto et al. 2012; Fukagawa et al. 2013). However, we should keep in mind that those structures can be naturally produced by magnetic structures, just as shown in our simulations. The spiral structures seen in our simulations are typically short-lived with lifetimes of the order of rotation time, e.g., 1000 yr at 100 AU for a disk around a central star with the solar mass. However, such structures are ubiquitously created and can almost always observed be somewhere in the simulated disks as shown in the movies for Figure 7 (online materials; also available at www.ta.phys.nagoyau.ac.jp/stakeru/research/glbdsk). For a detailed comparison with observations, we need to model the dust component in a reasonable way not only in the disk itself (Aikawa & Nomura 2006; Nomura & Nakagawa 2006) but also in wind regions (e.g., Heinzeller et al. 2011) since dust grains are expected to remain at high altitudes above the disk (Suzuki et al. 2010; McJunkin et al. 2014). A more detailed comparison with more realistic simulations with radiative transfer taking into account dust might be interesting in future work.

7. SUMMARY

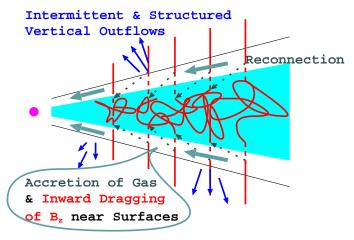


Fig. 35.— Schematic summary of the simulation results. The inward accretion of the gas mainly takes place in the surface regions. The net B_z (red lines) is also dragged inward in the surface regions, while in the midplane region the turbulence magnetic field stochastically moves inward and outward; namely B_z in the surface regions and B_z in the midplane continuously reconnect owing to the numerical resistivity (§5.4). Vertical outflows intermittently stream out by the Poynting flux (blue arrows).

We have performed 3D MHD simulations of global accretion disks threaded with weak vertical magnetic fields in the two types of the temperature profiles. In the simulations MHD turbulence is triggered and amplified by MRI, and in the saturated states the diagnostics for MRI, $-2\langle B_R B_\phi \rangle/B^2$ and $\langle B_R^2 \rangle/\langle B_\phi^2 \rangle$, are well correlated with the numerical resolutions as discussed in previous works (Hawley et al. 2011; Flock et al. 2011).

In addition, the effect of the different temperature profiles also affects the results through the vertical differential rotation. In the cases with spatially constant temperature (Case I), the rotation frequency is constant along the initial vertical field lines, and the overall properties of the MHD turbulence are similar to those observed in local shearing box simulations. On the other hand, in the cases with the profile of $T \propto 1/r$ (Case II), the gas in the surface regions rotates slower than the gas near the midplane. As a result, coherent magnetic fields are amplified in the surface regions, which also contribute to the Maxwell stress there.

This result indicates that thermal processes could play an important role in determining the saturation of the magnetic field and the properties of the turbulence in an accretion disk. In our simulations the temperature profiles are fixed, which implicitly assumes that external mechanisms such as irradiation from a central object regulate the temperatures. In other words, the thermodynamics determined by external mechanisms controls the dynamics of the disks. In reality, however, the temperature profile of a disk is also affected by internal mechanisms because the dissipation of the turbulence leads to the heating of a disk. A self-consistent treatment in determining the temperature distribution is necessary for our future studies.

The velocity fluctuations are dominated by the radial component and give $\approx 0.1-0.2$ of the sound speed around the midplane. The density fluctuations, $\delta\rho/\rho$ are also $\approx 0.1-0.2$. These values for the density and velocity perturbations are somewhat larger than those obtained in global simulations without initial vertical magnetic fields (Flock et al. 2011). In the case with $T \propto 1/r$, the regions with large $\delta\rho/\rho$, which coincide with the regions with large $-2\langle B_R B_\phi \rangle/\langle B^2 \rangle$ (high activities of MRI), are radially localized and stay for long times, which may be analogous to zonal flows seen in local simulations (Johansen et al. 2009). If applied to protoplanetary disks, such large density fluctuations are expected to influence the dynamics of dust particles.

The azimuthal power spectra of the magnetic fields show quite shallow power-law indice with respect to mode m, probably because the energy injection by the MRI is from the small scale (large m). On the other hand, the azimuthal power spectra of the velocity and density show $\propto m^{-1 \sim -2}$.

The onsets of intermittent and structured vertical disk winds are observed in the global simulations (Figures 8, 24, & 35), similar to that seen in the local simu-

lations (Suzuki & Inutsuka 2009; Suzuki et al. 2010). They are driven by the Poynting flux associated with the MHD turbulence. The magnetic pressure component gives the larger contribution than the magnetic tension component, which is in contrast to the local simulations in which both are contribute almost equally. Although the magnitude is smaller than that obtained in the local simulation, the injection regions of the magnetic tension form at $z\approx \pm 1.3H$. The acoustic waves, which are probably linked to the injection regions, are directed to the midplane. In protoplanetary disk conditions, these sound-like waves enhance the sedimentation of dust particles to the midplane.

In both Cases I & II, the mass accretions take place in the surface regions, because the α stresses are larger there. At the midplane the gas moves radially outward at a very slow speed. The velocity difference between the midplane and the surfaces may cause meridional circulation. Applied to protoplanetary disks, this causes the outward migration of solid particles at the midplane and possibly explains the observed crystalline dusts in the outer parts of disks. The radial motion of the vertical magnetic field lines also follows these tendencies of the gas, although the velocities of the magnetic fields and the gas are not the same because of the magnetic diffusion at the sub-grid scale. The magnetic flux is dragged inward in the surface regions, while at the midplane the turbulent magnetic flux moves stochastically outward and inward; the vertical magnetic fields continually reconnect at the sub-grid scales (Figure 35). However, we should carefully note that the observed layered accretion of the gas and the inward dragging of the vertical magnetic fields might be affected by the adopted boundary condition at the disk surfaces.

This work was supported in part by Grants-in-Aid for Scientific Research from the MEXT of Japan, 22864006 (TKS), 23244027, and 23103005 (SI). We thank the referee for many constructive comments. We are also grateful to Dr. Mario Flock, Dr. Xuening Bai, and Dr. Satoshi Okuzumi for many fruitful discussions. Numerical simulations in this work were carried out at the Yukawa Institute Computer Facility, SR16000 and at the Cray XT4 and XC30 operated in CfCA, National Astrophysical Observatory of Japan.

APPENDIX

SETTING INITIAL B_Z IN SPHERICAL COORDINATES

In our simulations, we use the method of constrained transport (Evans & Hawley 1988) in the spherical coordinates to handle the evolution of magnetic fields while keeping $\nabla \cdot \boldsymbol{B} = 0$. In order to set up the initial vertical magnetic fields (Equation 6) which exactly satisfy $\nabla \cdot \boldsymbol{B} = 0$ in all the cells, we use the vector potential, \boldsymbol{A} . To achieve the initial profile, $B_z \propto R^{-\mu/2} = (r \sin \theta)^{-\mu/2}$ for $\mu \neq 4$, we set

$$(A_r, A_\theta, A_\phi) = \left(0, 0, \frac{1}{2 - \mu/2} B_{z, \text{in}} \left(\frac{r \sin \theta}{r_{\text{in}}}\right)^{1 - \mu/2}\right). \tag{A1}$$

Then, we can set up the initial B from $B = \nabla \times A$, or in the explicit form,

$$(B_r, B_\theta, B_\phi) = \left(\frac{1}{r\sin\theta} \frac{\partial}{\partial \theta} (\sin\theta A_\phi), -\frac{1}{r} \frac{\partial}{\partial r} (rA_\phi), 0\right). \tag{A2}$$

In our simulations as well as other simulations adopting the constrained transport method, B are located at the face-centered positions and A are at the sides of each grid cell, and the discretization of Equation (A2) is straightforward.

Substituting Equation (A1) into Equation (A2) for confirmation, we can recover the required result,

$$(B_r, B_\theta, B_\phi) = (B_z \cos \theta, -B_z \sin \theta, 0), \tag{A3}$$

where $B_z = B_{z,\text{in}} \left(\frac{r \sin \theta}{r_{\text{in}}} \right)^{-\mu/2}$.

REFERENCES

Aikawa, Y., & Nomura, H. 2006, ApJ, 642, 1152 Bai, X.-N., & Stone, J. M. 2013a, ApJ, 767, 30 —. 2013b, ApJ, 769, 76 Balbus, S. A., & Hawley, J. F. 1991, ApJ, 376, 214 —. 1998, Reviews of Modern Physics, 70, 1 Beckwith, K., Hawley, J. F., & Krolik, J. H. 2009, ApJ, 707, 428 Blandford, R. D., & Payne, D. G. 1982, MNRAS, 199, 883 Bouwnan, J., Henning, T., Hillenbrand, L. A., et al. 2008, ApJ, 683, 479 Brandenburg, A., Nordlund, A., Stein, R. F., & Torkelsson, U. 1995, ApJ, 446, 741
Burgers, J. M. 1939, Verhand. Kon.Neder. Akad. Wetenschappen, Afd., Natuurkunde, Eerste Sectie, 17, 1 Afd., Natuurkunde, Eerste Sectie, 17, 1
Chandrasekhar, S. 1961, Hydrodynamic and hydromagnetic stability (Oxford: Clarendon)
Cho, J., & Lazarian, A. 2003, MNRAS, 345, 325
Clarke, D. A. 1996, ApJ, 457, 291
Davis, S. W., Stone, J. M., & Pessah, M. E. 2010, ApJ, 713, 52
Evans, C. R., & Hawley, J. F. 1988, ApJ, 332, 659
Flock, M., Dzyurkevich, N., Klahr, H., Turner, N., & Henning, T. 2012, ApJ, 744, 144
Flock, M., Dzyurkevich, N., Klahr, H., Turner, N. J., & Henning, T. 2011, ApJ, 735, 122
Fricke, K. 1968, ZAp, 68, 317
Fromang, S., Latter, H., Lesur, G., & Ogilvie, G. I. 2013, A&A, Fromang, S., Latter, H., Lesur, G., & Ogilvie, G. I. 2013, A&A, 552, A71 Fromang, S., Lyra, W., & Masset, F. 2011, A&A, 534, A107 Fromang, S., & Nelson, R. P. 2006, A&A, 457, 343 Fukagawa, M., Tsukagoshi, T., Momose, M., et al. 2013, PASJ, 65, L14 65, L14
Gammie, C. F. 1996, ApJ, 457, 355
Goldreich, P., & Schubert, G. 1967, ApJ, 150, 571
Goldreich, P., & Sridhar, S. 1995, ApJ, 438, 763
Guan, X., & Gammie, C. F. 2011, ApJ, 728, 130
Hashimoto, J., Tamura, M., Muto, T., et al. 2011, ApJ, 729, L17
Hawley, J. F. 2000, ApJ, 528, 462
Hawley, J. F., Gammie, C. F., & Balbus, S. A. 1995, ApJ, 440, 742 Hawley, J. F., Guan, X., & Krolik, J. H. 2011, ApJ, 738, 84
Hawley, J. F., Richers, S. A., Guan, X., & Krolik, J. H. 2013, ApJ, 772, 102
Heinzeller, D., Nomura, H., Walsh, C., & Millar, T. J. 2011, ApJ, 772, 112 731, 115 731, 115
Hirose, S., Blaes, O., & Krolik, J. H. 2009, ApJ, 704, 781
Hirose, S., Krolik, J. H., & Stone, J. M. 2006, ApJ, 640, 901
Io, Y., & Suzuki, T. K. 2014, ApJ, 780, 46
Iwasaki, K., & Inutsuka, S.-I. 2011, MNRAS, 418, 1668
Jacquet, E. 2013, A&A, 551, A75
Johansen, A., Youdin, A., & Klahr, H. 2009, ApJ, 697, 1269
Kato, Y., Hayashi, M. R., & Matsumoto, R. 2004, ApJ, 600, 338
Keller, C., & Gail, H.-P. 2004, A&A, 415, 1177
Kolmogorov, A. 1941, Akademiia Nauk SSSR Doklady, 30, 301
Kozlowski, M., Jaroszynski, M., & Abramowicz, M. A. 1978,
A&A, 63, 209 Kudoh, T., Matsumoto, R., & Shibata, K. 1998, ApJ, 508, 186Lesur, G., Ferreira, J., & Ogilvie, G. I. 2013, A&A, 550, A61

Lubow, S. H., Papaloizou, J. C. B., & Pringle, J. E. 1994, MNRAS, 267, 235
Lynden-Bell, D., & Pringle, J. E. 1974, MNRAS, 168, 603
Machida, M., Hayashi, M. R., & Matsumoto, R. 2000, ApJ, 532, Machida, M., & Matsumoto, R. 2003, ApJ, 585, 429 Machida, M., Nakamura, K. E., Kudoh, T., et al. 2013, ApJ, 764, Maeder, A. 1999, A&A, 347, 185 Matsumoto, R., & Tajima, T. 1995, ApJ, 445, 767 McJunkin, M., France, K., Schneider, P. C., et al. 2014, ApJ, 780, 150 Mościbrodzka, M., & Proga, D. 2009, MNRAS, 397, 2087 Muto, T., Grady, C. A., Hashimoto, J., et al. 2012, ApJ, 748, L22 Nelson, R. P., Gressel, O., & Umurhan, O. M. 2013, MNRAS, 435, 2010 Nelson, R. P., & Papaloizou, J. C. B. 2004, MNRAS, 350, 849 Nishikori, H., Machida, M., & Matsumoto, R. 2006, ApJ, 641, 862 Noble, S. C., Krolik, J. H., & Hawley, J. F. 2010, ApJ, 711, 959 Nomura, H., & Nakagawa, Y. 2006, ApJ, 640, 1099 Ohsuga, K., Mineshige, S., Mori, M., & Kato, Y. 2009, PASJ, 61, L7
Okuzumi, S., & Hirose, S. 2011, ApJ, 742, 65
— 2012, ApJ, 753, L8
Okuzumi, S., & Ormel, C. W. 2013, ApJ, 771, 43
Ormel, C. W., & Okuzumi, S. 2013, ApJ, 771, 44
Papaloizou, J. C. B., & Nelson, R. P. 2003, MNRAS, 339, 983
Parkin, E. R., & Bicknell, G. V. 2013a, ApJ, 763, 99
— 2013b, MNRAS, 435, 2281
Pessah, M. E., Chan, C.-k., & Psaltis, D. 2007, ApJ, 668, L51
Proga, D., & Begelman, M. C. 2003, ApJ, 592, 767
Rothstein, D. M., & Lovelace, R. V. E. 2008, ApJ, 677, 1221
Sano, T., Inutsuka, S., & Miyama, S. M. 1999, in Astrophysics and Space Science Library, Vol. 240, Numerical Astrophysics, ed. S. M. Miyama, K. Tomisaka, & T. Hanawa (Boston, MA: Kluwer). 383 Kluwer), 383 Sano, T., Inutsuka, S.-i., Turner, N. J., & Stone, J. M. 2004, ApJ, 605, 321 Shakura, N. I., & Sunyaev, R. A. 1973, A&A, 24, 337
Shi, J., Krolik, J. H., & Hirose, S. 2010, ApJ, 708, 1716
Simon, J. B., Hawley, J. F., & Beckwith, K. 2011, ApJ, 730, 94
Stone, J. M., Hawley, J. F., Gammie, C. F., & Balbus, S. A.
1996, ApJ, 463, 656 1996, ApJ, 463, 656
Stone, J. M., & Norman, M. L. 1992, ApJS, 80, 791
Stone, J. M., & Pringle, J. E. 2001, MNRAS, 322, 461
Suzuki, T. K., & Inutsuka, S.-i. 2006, Journal of Geophysical Research (Space Physics), 111, 6101
— 2009, ApJ, 691, L49
Suzuki, T. K., Muto, T., & Inutsuka, S.-i. 2010, ApJ, 718, 1289
Takeuchi, T., & Lin, D. N. C. 2002, ApJ, 581, 1344
Turner, N. J., Stone, J. M., Krolik, J. H., & Sano, T. 2003, ApJ, 593, 992 593, 992 Velikhov, E. P. 1959, Zh. Eksp. Teor. Fiz., 36, 1398 von Zeipel, H. 1924, MNRAS, 84, 665 Weber, E. J., & Davis, Jr., L. 1967, ApJ, 148, 217